Targeting the Hippo pathway in cancers via ubiquitination dependent TEAD degradation

Trang H. Pham[1♯], Kanika Bajaj Pahuja[1♯], Thijs J. Hagenbeek[1♯], Jason Zbieg[2], Cameron L. Noland[3], Victoria C. Pham[4], Xiaosai Yao[5], Christopher M. Rose[4], Kristen Browder[6], Ho-June Lee[1], Mamie Yu[1], May Liang-Chu[1], Scott Martin[1], Erik Verschueren[4], Jason Li[5], Marta H. Kubala[3], Rina Fong[3], Maria Lorenzo[3], Paul Beroza[7], Peter Hsu[3], Sayantanee Paul[1], Elisia Villemure[2], Wendy Lee[2], Tommy K. Cheung[4], Saundra Clausen[8], Jennifer Lacap[9], Yuxin Liang[4], Jason Cheng[9], Steve Schmidt[8], Zora Modrusan[4], Michael Cohen[10], James Crawford[2], Heinrich Jasper[6], Alan Ashworth[11], Jennie R. Lill[4], Shiva Malek[1], Joachim Rudolph[2], Ingrid E. Wertz[1], Matthew T. Chang[6*], Xin Ye[1*], Anwesha Dey[1*]

Departments of Discovery Oncology[1], Discovery Chemistry[2], Structural Biology[3], Microchemistry, Proteomics & Lipidomics[4], Bioinformatics[5], Immunology Discovery[6], Cheminformatics[7], Biochemical and Cell Biology[8], and Translational Oncology[9], Genentech, Inc., 1 DNA Way, South San Francisco, CA 94080, USA, Oregon Health and Science University, Portland, OR 97210, USA[10], Helen Diller Family Comprehensive Cancer Center, University of California San Francisco, San Francisco, CA 94158, USA[11]

♯These authors contributed equally to this work

* To whom correspondence should be addressed

E-Mails: dey.anwesha@gene.com, ye.xin@gene.com, matthew.chang1@gmail.com

ABSTRACT

The Hippo pathway is among the most frequently altered key signaling pathways in cancer. TEAD1-4 are essential transcription factors and key downstream effectors in the Hippo pathway. Here we identified RNF146 as a ubiquitin ligase (E3) that can catalyze TEAD ubiquitination and negatively regulate their function in cells. We show that this ubiquitin of TEADs is governed by their PARylation state and validated the genetic interaction between RNF146 and the Hippo pathway in cancer cell lines and the model organism *Drosophila melanogaster.* Furthermore, we demonstrate that pharmacologically induced ubiquitination of TEADs by heterobifunctional chemical inducers of protein degradation (CIDE) molecules can promote potent pan-TEAD degradation. These TEAD-CIDEs can effectively suppress activation of TEAD target genes in a dose-dependent manner and exhibited significant anti-proliferative effects in Hippo-dependent tumor cells, thus phenocopy the effect of genetic ablation of TEAD protein. Collectively, this study demonstrates a post-translational mechanism of TEAD protein regulation and provides a proof-of-concept demonstration that pharmacological induced TEAD ubiquitination could be an effective therapeutic strategy to target Hippo-driven cancers.

INTRODUCTION

The genetic alterations of Hippo pathway components has been observed in 10% of human cancers including glioma, breast, liver, lung, prostate, colorectal, and gastric cancers (Dong et al., 2007; Sanchez-Vega et al., 2018; Steinhardt et al., 2008; Zhao et al., 2007). In addition, non-genetic dysregulations of the pathway are broadly involved in tumor development (Dey et al., 2020; Zanconato et al., 2016). These upstream dysfunctions converge on TEAD transcription factors as a central node to regulate transcriptional output driving tumor progression, metastasis, immunity, cancer metabolism, and drug resistance (Cordenonsi et al., 2011; Halder and Johnson, 2011; Kapoor et al., 2014; Lin et al., 2015; Yu and Guan, 2013). There are four TEAD members in humans, TEAD1 (TEF-1/NTEF), TEAD2 (TEF-4/ETF), TEAD3 (TEF-5/ETFR-1), and TEAD4 (TEF-3/ETFR-2/FR-19) (Lin et al., 2017; Yasunami et al., 1996) that share high structural similarity and a conserved palmitoylation pocket (Calses et al., 2019; Huh et al., 2019; Lin et al., 2017). Even though TEADs are mostly chromatin-bound in cells (Li et al., 2015), they do not exhibit any transcriptional activity on their own and rely on their coactivators to turn on gene expression (Xiao et al., 1991). Conversely, the two main Hippo

pathway transcription effectors, YAP (*YAP1*) and TAZ (*WWTR1*), control gene expression via interacting with TEADs at their C-terminal transactivating domains (Vassilev et al., 2001; Zhang et al., 2009; Zhao et al., 2008).

Consistent with TEADs' central roles in controlling the Hippo pathway output, genetic studies revealed that TEADs play important roles during development, including cardiogenesis, neural development, and trophectoderm lineage determination (Chen et al., 1994; Huh et al., 2019; Kaneko et al., 2007; Nishioka et al., 2009; Nishioka et al., 2008; Yagi et al., 2007; Yasunami et al., 1996). Further more numerous studies underline the importance of TEADs in human cancers. Overexpression of TEADs has been implicated in multiple stages of cancer progression across cancer types. Moreover, the Hippo pathway has been showing as a common mechanism of resistance to chemo- and targeted therapies (Kapoor et al., 2014; Lin et al., 2015; Song et al., 2015). To date, multiple efforts to target the Hippo pathway in cancers have mostly focused on small molecules binding to the palmitoylation pocket of TEAD, which can subsequently block the interaction between YAP/TAZ and TEADs (Calses et al., 2019; Dey et al., 2020).

Recent innovations in the field of targeted protein degradation and manipulation of the ubiquitin-proteasome system have enabled new therapeutic approaches (Scheepstra et al., 2019). Targeted protein degradation using heterobifunctional chemical inducers of protein degradation (CIDEs), also known as PROTACs (Sakamoto et al., 2001) to target challenging oncogenic targets have emerged as a new frontier of drug discovery (Chamberlain and Hamann, 2019; Yang et al., 2019). Such heterobifunctional degraders consist of two moieties, one binding to the target protein and the other to a E3 ubiquitin ligase to induce proximity between the E3 ubiquitin ligase with the target, thus cause ubiquitination and subsequent proteasomal degradation of the target protein. Such degrader molecules offer several advantages over small molecule inhibitors. They act through an event-driven mechanism instead of conventional occupancy-driven pharmacology, in addition, target protein degradation removes all functions of the target protein and may also lead to destabilization of entire multidomain protein complexes (Chamberlain and Hamann, 2019; Yang et al., 2019). Heterobifunctional degraders have been reported for a diverse array of oncoproteins, and some of them have entered clinical trials (Han et al., 2019; You et al., 2020).

In this study, we explored intrinsic and induced TEAD regulation via the ubiquitin-proteasome system as a way to suppress the function of TEAD proteins. We identified PARylation-dependent ubiquitin ligase RNF146 as an endogenous ubiquitin ligase for TEAD transcription factors. We further demonstrate that RNF146 is a potent negative regulator of TEAD transcriptional activity, indicating that TEAD ubiquitination can be explored to suppress the Hippo target gene activation upon YAP/TAZ stabilization (Fan et al., 2020). To this end, we report the discovery and characterization of a TEAD-CIDE, compound D, that can induce potent and sustained degradation of all four human TEAD isoforms by co-opting the CRL4-CRBN ubiquitin ligase complex. Compound D exhibits significant inhibition of cell proliferation and downstream signaling compared to compound A, a reversible TEAD lipid pocket binder that lack the ubiquitin ligase binding moiety. As a proof-of-concept, we show that TEAD-degrader-induced degradation had comparable anti-proliferation effects as genetic TEAD depletion mediated by sgRNA or siRNA in Hippo pathway-dysregulated cell lines. Collectively, our study demonstrates that ubiquitination of TEADs via RNF146 or by TEAD-CIDE-induced CRL4-CRBN recruitment is an effective mechanism to suppress activation of the Hippo pathway target genes. This work highlights previously unrecognized crosstalk of TEAD ubiquitination and PARylation and a new strategy for targeting the Hippo pathway in cancers.

RESULTS

TEAD transcription factors are ubiquitinated in cells

To assess post-translational modifications that could impact TEAD stability, in particular ubiquitination, we transfected HEK-293 cells with expression vectors for each of the four TEAD paralogs followed by a cell-based ubiquitination assay. Our results indicated that all four paralogs can be ubiquitinated in cells (Figure 1A), albeit at different levels. Focusing on TEAD4 as a representative example, we found that its ubiquitination levels were further increased upon treatment with proteasome inhibitor MG132 in a time-dependent manner (Figure 1B), suggesting that a fraction of TEAD4 ubiquitination can result in proteasomal degradation. To further assess ubiquitination of endogenous proteins, we performed a peptide level immunoaffinity enrichment (PTMScan) experiment to assess the profiles of K-GG peptides (result of trypsin digestion of ubiquitinated proteins) for endogenously expressed TEAD4 (Figure 1C). We identified several ubiquitination sites (Figure 1D) and mapped them on TEAD4 using known crystal structures. These ubiquitination sites did not reside in any specific TEAD structural domain (Figure S1A, B)

(Mesrouze et al., 2017; Shi et al., 2017). Consistent with our cell-based ubiquitination assay (Figure 1B), the ubiquitinated peptides were significantly increased following MG132 treatment (Figure 1E, S1C and Supplemental Table 1). Furthermore, we observed multiple ubiquitin linkages in IP-mass spectrometry studies with endogenous TEAD4 including K48-linked ubiquitin that is known to target the modified protein for proteasomal degradation (Table 2). Taken together, our data demonstrates that the TEAD transcription factors can be poly-ubiquitinated in cells, and such poly-ubiquitination may target TEADs for proteasomal degradation and/or modulate the transcriptional activity of TEADs.

RNF146 is an E3 ligase for TEAD transcription factors and negatively regulates TEAD transcriptional activity

We next sought to identify the ligase responsible for TEAD ubiquitination. We performed a screen using a siRNA library for 640 ubiquitin-related genes in the MCF7 cells that carries a luciferase reporter driven by multimerized TEAD binding sites (8xGTIIC-Luc). We identified three ubiquitin ligases – RNF146, TRAF3, and PHF5A – as potential negative regulators for the Hippo pathway from the primary screen using the luciferase reporter (Supplemental Table 3 and Figure S2A). Next, we validated these hits by assessing their impact on the TEAD target genes CTGF and CYR61 upon gene knockdown mediated by siRNA (Figure S2B). Two independent siRNAs targeting RNF146 consistently enhanced the expression of both genes, again indicated *RNF146* as a putative negative regulator of TEAD-mediated gene expression (Figure 2A and S2B).

RNF146 had been previously reported to positively regulate YAP activity through degradation of AMOTs (Wang et al., 2015). To understand this discrepancy with our finding, we leveraged whole-genome dependency screen results from DepMap to broadly assess the loss-of-function effect of RNF146 across cancer cell lines (Meyers et al., 2017). We systematically mapped the functional interactome of the Hippo pathway by assessing the correlation between the loss-of-function effect of individual genes (measured by their Chronos scores) with that of the known Hippo pathway components across a large panel of 739 cancer cell lines. As a positive control, we captured strong positive correlations between WWTR1/TAZ versus known negative regulators of the Hippo pathway including *NF2*, *LATS2*, *AMOTL2*, and *MAP4K*. Intriguingly, we found that the *RNF146* Chronos score anti-correlated with the Chronos scores of TEAD1 and WWTR1/TAZ similarly to these known negative regulators (Figure 2B). Taken together, this provided

orthogonal evidence for E3 ligase RNF146 as a putative negative regulator of the Hippo pathway transcription effectors in TEAD-dependent cancer cell lines.

To further assess the function of RNF146, we depleted RNF146 by either sgRNA or siRNA. We observed significant reduction of TEAD4 poly-ubiquitination (Figure 2C and S2C). Additionally, we performed RNA-seq and examined the effects of *RNF146* knockdown on the transcription output by YAP/TAZ-TEAD using a published Hippo signature (Pham et al., 2021). We found that siRNF146 led to up-regulation of Hippo signature genes, while siYAP1 led to down-regulation of the Hippo signature. (Figure 2D and S2D, E and F). This is consistent with the role of YAP1 as a transcriptional coactivator for TEAD while RNF146 negatively regulates TEADs. We further examined whether RNF146 interacts with TEAD by performing immunoprecipitation using a Myc tagged TEAD4 construct. This demonstrated once again that TEAD4 interacts with endogenously expressed RNF146 (Figure 2E). Additionally, we observed significant stabilization of TEAD4 under RNF146 depletion by siRNA and sgRNA in multiple cell lines (Figure S2G-I). Notably the effect on TEAD1 was lower, consistent with lower ubiquitination level of TEAD1 (Figure 1A). We also confirmed that RNF146 and full-length nuclear TEAD4 are present in complex by performing a proximity ligation assay (PLA) using antibodies specific to each protein (Figure S3A-D). Taken together, our studies demonstrate that RNF146 interacts with TEAD4, induces TEAD4 poly-ubiquitination, and negatively regulates TEAD-mediated gene transcription.

The ubiquitination of TEAD is associated with PARylation.

RNF146 has been reported to be a poly (ADP-ribosyl)ation (PARylation)-dependent E3 ubiquitin ligase (Kang et al., 2011; Zhang et al., 2011; Zhou et al., 2011). Therefore, we examined whether TEAD ubiquitination was also associated with PARylation. IP-mass spectrometry studies with endogenous TEAD4 identified two members of poly (ADP-ribose) polymerases including PARP1, and PARP9 (Figure 3A and Supplemental Table 4). As PARP9 is a mono-ADP-ribosylation enzyme, and only PARylates ubiquitin, we focused on PARP1 (Yang et al., 2017). First, we confirmed the interaction between TEAD4 and PARP1 by IP and Western blot (Figure 3B). Next, we transfected TEAD expression constructs into HEK293 cells and blotted immunoprecipitated TEAD transcription factors with an anti-PAR antibody to confirm their PARylation (Figure 3C). Furthermore, we demonstrated that TEAD4 ubiquitination is partially

dependent on PARP1, as *PARP1* depletion using sgRNA reduced TEAD4 ubiquitination levels (Figure 3D and S3E). While these results indicate PARP1 is likely responsible for TEAD4 PARylation and subsequent ubiquitination, the incomplete loss of TEAD4 ubiquitination suggests potential roles of other PARPs and PARylation-independent mechanisms of ubiquitination in the process as well.

PARylation has been reported to play diverse roles in the DNA damage response (DDR), DNA repair, transcription, replication, chromatin remodeling, metabolism, and cell death (Kamaletdinova et al., 2019). To pinpoint the PARylation site on TEADs and further dissect the relationship between TEAD PARylation and ubiquitination, we leveraged previous proteome-wide mass spectrometric studies for PARylation (Jungmichel et al., 2013; Zhang et al., 2013) and identified PARylation of a conserved aspartate (Asp70) site on TEAD 1-4 in the TEAD DNA binding domain (Shi et al., 2017). Notably, this site is distal from the DNA binding surface and lies in the linker region between two α-helices that interacts with the DNA (Figure 3E). Intriguingly, mutating Asp70 to an alanine (Ala) significantly decreased TEAD4 PARylation (Figure 3F) and ubiquitination (Figure 3G) and extended TEAD4 half-life (Figure S3F). Taken together, these data suggest that PARylation by PARP-family proteins could mark TEAD4 for ubiquitination by PARylation-dependent E3 ubiquitin ligase RNF146.

RNF146 is a negative regulator of the Hippo pathway in *Drosophila melanogaster*

The Hippo pathway is conserved in *Drosophila melanogaster* and mammals (Halder and Johnson, 2011; Pan, 2010; Sudol and Harvey, 2010; Zhao et al., 2010). Given the sequence similarity of *Drosophila* Scalloped (Sd) and mammalian TEAD1-4, including the conserved Asp70 residue (Figure 4A), we examined the genetic interaction between *RNF146* and the Hippo pathway in *Drosophila* using the tissue over-growth phenotype of Hpo loss-of-function conditions (Udan et al., 2003).

First, we induced Hpo loss-of-function in the developing eye by expressing a dsRNA against Hpo using ey::Gal4. This resulted in significantly larger eyes with additional folding of the cuticle behind the eyes compared to luciferase RNAi as a control. We confirmed that Sd is required for eye over-growth in Hpo loss of function conditions, as Hpo knockdown did not increase eye size in Sd RNAi expressing animals (Fig. S4A, B). These phenotypes are consistent

with inactivation of the Hippo pathway kinase cascade resulting in nuclear localization of Yki which then binds Sd to activate cell proliferation. In such a Hpo loss-of-function background, we found that overexpression of RNF146 rescued the overgrowth phenotype and resulted in significantly smaller eyes, supporting its role as a negative regulator of the transcriptional program downstream of Sd (Figure 4B, C). Conversely, RNF146 knockdown increased eye size further in animals expressing Hpo RNAi, indicating that RNF146 can negatively regulate the activity of Sd/Yki and limit their full activation in Hpo loss of function conditions (Fig. S4C, D). Next, we assessed the genetic interaction between RNF146 and Hpo using an eyFLP system (Newsome et al., 2000) to generate *hpo*^{KC202} mutant clones and overexpress RNF146 in a genetic background in which non-clonal cells (twinspots) are eliminated by the presence of GMR::Hid (Newsome et al., 2000). Using this system, we again observed that overexpression of RNF-146 suppresses the overgrowth phenotype of Hpo mutant clones compared to wild type clones (Figure 4D, E). Of note, overexpression of RNF146 alone resulted in a modest increase in eye sizes compared to luciferase RNAi control (Fig. 4C). This is in contrast to the anti-growth effect of RNF-146 in the Hpo loss-of-function background and indicates RNF146 may regulate other genes/pathways controlling eye sizes besides its role as a negative regulator of Sd/yki activity. Taken together, the genetic interaction between RNF146 and Hpo in *Drosophila* eyes demonstrate that RNF146 functions as a negative regulator of over-growth phenotype associated with dysregulation of the Hippo pathway, consistent with our earlier computational and experimental results in human cell line models described above.

Of note, we also attempted to assess the genetic interactions between Sd and RNF146 with overexpression assays. Consistent with previous reports (Simmonds et al., 1998; Zhao et al., 2008), overexpression of the fly homolog of TEAD Sd resulted in a dominant-negative anti-growth phenotype (Figure S4E). Intriguingly, co-overexpression of Sd and RNF146 seems to enhance such dominant-negative effect into a cell-lethal phenotype, as only a few animals emerged from such crosses and these animals had no eyes (Fig. S4E). These results indicate interaction between RNF146 and Sd in *Drosophila* is complex and require additional studies to fully resolve.

TEAD1/2/3/4 down-regulation suppress cell proliferation and Hippo pathway signaling

Deregulation of Hippo signaling pathway has been implicated in a variety of human cancers. To understand the effects of TEAD loss, we performed *TEAD1-4* knockdown to determine TEAD dependency across a spectrum of cancer cell lines. We confirmed *TEAD1-4* knockdown via TaqMan RT-qPCR and Western blotting 3 days after transfection (Figure S5A and S5B) and assessed cell proliferation using the Cell Titer Glo assay. *TEAD1-4* knockdown resulted in downregulation of the Hippo pathway signature gene *CTGF* (Figure S5A) suggesting the pathway was altered. *TEAD1-4* knockdown resulted in a significant reduction in cell proliferation in all cell lines tested except two negative control Hippo-independent cell lines SK-N-FI and HCSC-1, which lack *YAP/WWRT1* expression (Figure 5A). We further confirmed TEAD dependency *in vivo* using xenograft studies in mice. Mice (n=10) that were injected with MDA-MB-231 cells showed significant reduction in tumor volume upon induced *TEAD1-4* knockdown in an intervention setting (Figure 5B and S5C-D). Taken together, these results indicate depletion of TEADs as an anti-cancer therapeutic strategy in Hippo-dependent cell lines.

Development and Screening of pan-TEAD lipid pocket degraders

In cells, TEAD transcription factors can be very stable (Pham et al., 2021). We reasoned that the very low turn-over rate, the intermediate step of being PARylated, as well as different ubiquitination levels of all four TEAD paralogs (Figure 1A and S2G) may limit the ability of RNF146 and potentially other endogenous E3-ligase in reducing TEAD protein levels in cells. Thus, we sought to deplete TEAD proteins by directly target them for ubiquitination and proteasomal degradation via pharmacologically inducing interactions between TEAD and other abundantly expressed and PARylation-independent E3 ligases.

To this end, we designed and synthesized a series of heterobifunctional TEAD CIDEs based on reversible TEAD lipid pocket binding ligand compound A and B with several E3 ligase ligands (compound C-E in Figure 5C and compound F-K in Figure S5E). Compound A is a close in analog of Compound B as described previously (Holden et al., 2020). Compound A binds the same site as Compound B in a very similar manner and the only modifications to Compound B were made to include a handle to attach an E3 Ligase ligand. These compounds have been previously disclosed in patent application: WO2020051099. To facilitate structure-based design of potent TEAD degraders, we solved the co-crystal structure of compound A bound to TEAD2 (Figure 5C, D). As expected, based on previous reports and our

biochemical data, this compound strongly binds all the TEAD isoforms via the lipid pocket in a TEAD lipid HTRF assay. Compound A makes hydrogen bonds to the backbone amides of Cys380 and Glu381, but binding appears to be driven primarily by van der Waals interactions deep in the pocket as well as with the benzyl group, which is sandwiched between Cys380 (which would otherwise be lipid-modified) and Lys357 (Figure 5D). This moiety provides an optimal vector for the terminal amide to exit the pocket, allowing for conjugation of an E3 ligase ligand via a linker in our TEAD-CIDEs (Figure 5D and S5E). A set of TEAD CIDEs were evaluated, containing ligands that bind the ubiquitin ligases XIAP, CRL2-VHL, and CRL4-CRBN. Reversible TEAD lipid pocket ligands, compound A and compound B, both bind pan-TEAD but show no inherent cellular activity in the TEAD dependent OVCAR8 cell line (Figure 7A). These two compounds were selected as non-degrader control compounds (Figure 5C). Gratifyingly, TEAD-CIDEs based on compound A maintained good pan-TEAD biochemical potency when linked to all three evaluated ligase ligands. Additionally, TEAD/CRBN CIDEs led to significant activity in our cellular OVCAR-8 antiproliferation assay (Figure 5C). Based on these data, compound D and compound E were selected for further evaluation. We attempted to obtain co-crystal structures of TEAD, CRBN, and either of the compounds but were unsuccessful, likely owing to the highly flexible nature of the PEG linkers in our compounds.

Through multiplexed mass spectrometry-based global proteomics in MDA-MB-231 cell line, we next assessed compound D and compound E for TEAD specificity and selectivity. We identified significant downregulation of shared as well as unique TEAD peptides (TEAD1, 3) when cells were treated with compound D and compound E for both 4 h and 8 h compared to compound A (Figure 5E and S5F). Other than TEAD peptides, we noted that PDE6δ (Retinal rod rhodopsin-sensitive cGMP 3',5'-cyclic phosphodiesterase subunit delta) and RNF166 (Ring finger protein 166) as the only other significantly reduced proteins (Figure 5E and S5F). RNF166 has been previously identified as a target of other CRBN-based ligands (lenalidomide) and degraders (You et al., 2020), indicating it could be a off-target for the CRBN binding portion of Compound D and Compound E. As expected, the parent ligand compound A did not induce any significant changes in protein abundance, indicating TEAD degradation induced by CIDEs depends E3 ligase recruitment.

CIDE-induced TEAD degradation is dependent on CRBN modulation and the proteasome

We next evaluated and confirmed that both compound D and compound E induced TEAD degradation in TEAD-dependent cell lines in a concentration- and time-dependent manner (Figure 6A, B, Fig S6A). No TEAD degradation was observed upon treatment with a TEAD lipid pocket binder (compound A or compound B) indicating that both TEAD and CRBN engagement are required for CIDE-mediated TEAD degradation (Figure 6A and S6B). In addition, we confirmed PDE6δ degradation with compound D (Figure 6A). Based on this degradation, we docked compound A into the crystal structure of the PDE6δ ligand binding pocket (PDB ID: 5ML2) and found that it could occupy that pocket without significant clashes (Figure S6C) (Tian et al., 2010). However, from genome-wide CRISPR screen (Meyers et al., 2017), PDE6δ dependency was not correlated with other Hippo pathway members (Figure S6D, E) and was not essential in the TEAD-dependent cell lines tested here suggesting that PDE6δ loss would not lead to anti-growth effects in the TEAD-dependent cell lines used in our study.

Next, we treated cells with proteasome and ubiquitin ligase E1 inhibitors. Co-treatment of cells with compound D /compound E with MG132 (a proteasome inhibitor) or MLN7243 (an E1 inhibitor) prevented TEAD degradation (Fig 6C, 6D), indicating that the proteasome pathway is required for effective CIDE-mediated degradation. To confirm that compound D and compound E-induced TEAD degradation is CRBN-dependent, we performed siRNA knockdown of *CRBN* in MDA-MB-231 and evaluated TEAD degradation with 0.1 μM and 0.5 μM of compound D for 16 hours (Figure 6E). Overall, the data shows that TEAD-CIDEs mediated TEAD degradation is dependent on the ubiquitin/proteasome pathway and the CRL4-CRBN ubiquitin ligase.

TEAD-CIDEs inhibit proliferation and downstream signaling in Hippo pathway dependent cell lines

In order to assess the anti-proliferative effect of TEAD-CIDEs, we tested compound D and compound E in OVCAR-8 and SK-N-FI (*YAP/WWTR1* deficient, Hippo pathway independent) cells. Both TEAD-CIDEs resulted in a decrease in cell proliferation in OVCAR-8 cell line and did not have anti-proliferative effects in SK-N-FI (Figure 7A, 7B). No anti-proliferative effect was observed with compound A or compound B, suggesting that this effect was degradation-dependent (Figure 7A, 7B). Similar effects were observed in crystal violet growth assay (Figure 7C, 7D). The anti-proliferative effect of compound D was further validated across a spectrum of Hippo pathway dependent cell lines

(Figure S7A, S7B). Given the enhanced anti-proliferative effects of compound D as compared to compound A, we next evaluated its effects on Hippo pathway output by RNA-Seq. Compound D treatment resulted in robust concentration dependent downregulation of Hippo pathway target genes as compared to compound A (Figure 7E, and 7F). Taken together, our data serve as a proof-of-concept that TEAD proteins can be pharmacologically targeted and modulated through the ubiquitin-proteasomal system.

TEAD CIDE specifically reduced chromatin accessibility at TEAD motifs

To assess whether TEAD-CIDE could lead to remodeling of the chromatin, we performed ATAC-seq on OVCAR-8 cells treated with Compound D or DMSO control for 48 hours. Differential peak analysis detected 4394 gained, 9482 lost and 132803 unaltered regions (absolute logFC >1 and FDR < 0.01, negative binomial test) (Figure 8A). Both the gained and lost regions were found predominantly at distal regions (Figure 8B). We observed significant reductions in chromatin accessibility at the promoter and multiple enhancer regions of well-known TEAD targets such as ANKRD1 and CCN1 (aka. CYR61) (Figure 8C).

Using systematic unbiased motif enrichment analysis, we found that regions which were associated with loss of chromatin accessibility were significant enriched for TEAD DNA binding motifs (Figure 8D). Since the majority of the downregulated peak regions were distal, we assigned enhancer-gene targets using links derived from aggregated chromatin capture data by Poly-Enrich. The most significantly enriched pathway corresponded to Cordenonsi_YAP_conserved_signature. This suggests that the observed downregulation of Hippo pathway target genes is likely due to the loss of TEAD-associated chromatin accessibility *in vitro*. Interestingly, we noted, among the ten most downregulated pathways, many were related to cell adhesion (Figure 8E), which has been previously associated with YAP/TAZ biology. Given that these pathways were modulated through the loss of TEAD-associated chromatin accessibility, together this study suggests that TEAD is a critical conduit of Hippo pathway activity. Loss of TEAD protein through degradation can potently alter the chromatin landscape of Hippo-driven cancers. Collectively, this highlights TEAD degraders as valuable tools to uncover the role of TEAD accessibility in cancers to guide future drug development efforts.

DISCUSSION

In this study, we show that the activity of TEAD transcription factors can be post-transcriptionally regulated via the ubiquitin/proteasome system. We demonstrate that TEAD proteins can be poly-ubiquitinated (Figure 1) and identify RNF146 as an E3 ligase for TEADs (Figure 2). Such ubiquitination is dependent, at least in part, on TEAD PARylation by the PARP-family members (Figure 3). Our study also demonstrated the genetic interaction of RNF146 with the Hippo pathway in *Drosophila melanogaster*, establishing RNF146 as a conserved negative regulator of the Hippo pathway across species (Figure 4). In addition, we observed that RNF146 over expression induced an over-growth phenotype on its own, which will require future investigation and imply a role of RNF146 in developmental homeostasis in general.

RNF146 has been previously reported as a PARylation-dependent ubiquitin ligase (Kang et al., 2011; Zhang et al., 2011; Zhou et al., 2011). TEAD transcription factors have been previously reported as targets of PARylation, which in turn impact their DNA binding activity (Butler and Ordahl, 1999; Jungmichel et al., 2013; Zhang et al., 2013). The conserved Asp70 PARylation-target residue, as well as other Asp residues in the DNA-binding domain, do not reside in the DNA-binding interface of TEAD4 whereas ubiquitinated Lysine residues do. Thus, we speculate that PARylation of TEAD may indirectly impact DNA-binding through ubiquitination, rather than directly affecting DNA-binding. This raises the possibility that ubiquitination by RNF-146 may directly modulate TEAD activity in addition to marking them for proteosome mediated degradation. However, the requirement of PARylation as the intermediate step between RNF146 and TEAD, the exact interaction interface between RNF146 and TEAD, and the direct versus indirect role of ubiquitination in regulating TEAD transcriptional activity will require future genetic and biochemical studies in diverse models.

Of note, previous studies demonstrated that RNF146 may positively regulate YAP activity through degradation of AMOTs (Wang et al., 2015). However, our study demonstrates RNF146 functions as an E3 ligase and negative regulator of TEADs. We speculate the different modes of RNF146 action could be influenced by the cellular context, its subcellular localization, and PARylation status of different RNF146 substrates. Furthermore, our analysis of pan-

cancer gene dependency revealed a clear function of RNF146 as a negative regulator of YAP/TAZ/TEAD across many cancer cell lines of diverse indications (Fig. 2B).

TEADs are central components of the transcriptional machinery controlled by the Hippo pathway. Genetic depletion of TEADs induces strong anti-proliferative effects in Hippo-dependent cancer cell lines. While we identified RNF146 as an E3 ligase for TEAD transcription factors, knockdown of RNF146 had limited effects on TEAD stability in cancer cells. This prompted us to further explore pharmacologically engage other ubiquitin ligases and the proteasome system as a mean to limit the activity of all TEAD isoforms using CIDEs to therapeutically target the Hippo pathway. To this end, we designed, synthesized and evaluated a series of potent heterobifunctional TEAD-CIDEs based on reversible TEAD lipid pocket binding ligand compound A. As a proof-of-concept study, we engineered TEAD-CIDEs (compound D, compound E) that were able to reduce TEAD protein levels in a CRBN-dependent manner with concentrations as low as 0.1 μM. CIDE-induced TEAD degradation resulted in significant concentration- and time-dependent reduction in downstream Hippo signaling genes in Hippo pathway dysregulated cells. This study demonstrated, to our knowledge, the first class of TEAD degraders that specifically inhibit cell proliferation and suppress Hippo downstream signaling validates TEAD degraders as a potential therapeutic modality to target the Hippo pathway.

We identified PDE6δ as an off-target protein for these TEAD-CIDEs. Structural biology studies suggest that while the pockets of TEAD and PDE6δ are quite different, PDE6δ may still be able to accommodate certain classes of TEAD ligands and should be considered as a potential off-target for TEAD lipid pocket-binding molecules (Tian et al., 2010). While PDE6δ loss is unlikely to impact the observed Hippo pathway specificity, next-generation TEAD-CIDEs should be engineered to achieve higher TEAD lipid pocket binding specificity and degradation efficiency. Further development of TEAD-CIDEs is needed to optimize the pharmacological properties to enable *in vivo* testing.

In summary, we have identified an important mechanism of regulating TEAD protein levels by the ubiquitin/proteasome system and demonstrated that this can be pharmacologically enhanced through TEAD-CIDEs.

TEAD-CIDEs serve as potent chemical probes for studying the effects of pan-TEAD degradation for potential therapeutic intervention. As many cancer targets lack enzymatic function, CIDEs enable a tractable option to convert inactive ligands to functional degraders. This study provides further proof-of-concept for degraders as a therapeutic strategy for targeting challenging and hard to drug pathways in cancer.

FIGURE LEGENDS

Figure 1. TEAD transcription factors are ubiquitinated and targeted for proteasomal dependent degradation. (A) TEADs are ubiquitinated. HEK 293 cells were transfected with TEADs-Myc and V5-ubiquitin plasmids for 48 hours, followed by immunoprecipitation with an anti-V5 antibody. TEADs expression and ubiquitinated TEADs were detected with anti-Myc antibody (n=3). **(B)** MG132 induces accumulation in TEAD ubiquitination. HEK 293 cells were transfected with TEADs-Myc and V5-ubiquitin plasmids for 48 hours followed by immunoprecipitation with anti-V5 antibody after additional treatment of 10 µM of MG132. TEADs expression and ubiquitinated TEADs were detected with anti-Myc antibody (n=3). **(C-E)** Ubiquitination sites on TEAD4 were mapped using KGG motif immunoprecipitation, followed by LC-MS/MS. For schematic in C, TEAD4-Myc was overexpressed in HEK293 cells for 48 hours with or without 10 µM of MG132 for 6 hours. KGG motif immunoprecipitation was then performed followed by LC-MS/MS. * represents each ubiquitination site. In D, predicted Lysine sites of ubiquitination is in the summary table. In E, ubiquitination for TEAD4 across conditions (red line) represents the aggregate of individually quantified K-GG peptides (black lines) using a linear mixed-effect model. Each quantification event represents the non-redundant, absolute peak area (converted to log2) under a given condition for a confidently assigned K-GG peptide spectral match.

Figure 2. RNF146 is a putative ubiquitin ligase for TEADs. **(A)** RNF146 was identified from our E3 ligase screen using siRNA libraries targeting ubiquitin-related genes. siRNA libraries targeting 1088 ubiquitin-related genes were transfected to assess the effects on MCF7-TEAD reporter activity (n=2) as described in the method. All seven siRNAs of RNF146 were identified from the screen. The x-axis represents the calculated robust Z-score and y-axis represent the number of siRNAs per bin. **(B)** RNF146 is a negative regulator of the Hippo pathway. Achilles dependency network of YAP/TAZ (Nodes are significantly correlated genes, genes that are significantly correlated are connected by a line.

Colors of nodes denote 2 distinct clusters based on random walk algorithm). An example of the RNF146 Chronos score is negatively correlated with the Chronos score of *WWTR1* and positively correlated with Chronos scores of *NF2*. **(C)** TEAD ubiquitination is reduced upon knockdown of *RNF146*. After 24 hours of siRNF146 treatment, TEADs-Myc and V5-ubiquitin were transfected into HEK293 cells for an additional 48 hours and *in vivo* ubiquitination assay was performed as described in Figure 1. TEADs expression and ubiquitinated TEADs were detected with anti-Myc antibody. RNF146 knockdown was confirmed via quantitative RT-PCR (n=3). **(D)** RNF146 negatively regulates the Hippo signature. OVCAR8 cells were transfected with siRNAs for *RNF146*, *YAP1* as indicated for 48hrs. RNA-seq was performed and Hippo signature was examined. **(E)** TEAD interacts with RNF146. HEK 293 cells were transfected with TEAD4-Myc for 48 hours, TEAD4 pull-down was then performed with an antibody that recognizes Myc-tag. TEAD4 expression and RNF146 interaction were detected using Myc antibody and RNF146 antibody respectively.

Figure 3. The ubiquitination of TEADs is dependent on their PARylation state. (A) TEAD transcription factors interact with multiple members of the PARP family including PARP1 and PARP9. IP Mass-spec was done in Patu-8902 cell line using a pan-TEAD antibody which detects and pulls down all four TEAD isoforms. IgG antibody was used as a control for immunoprecipitation. The numbers represent peptide counts. Condition 1 was in the shNTC cell line, condition 2 was in the sh*YAP1/WWTR1* cell line and the interaction was detected in both conditions. **(B)** TEAD4 interacts with PARP1. HEK 293 cells were transfected with TEADs-Myc plasmid for 48 hours followed by immunoprecipitation with anti-Myc antibody. PARP1 expression was detected with an anti-PARP1 antibody (n=3). **(C)** TEADs are PARylated. HEK 293 cells were transfected with duo tagged TEAD-Myc-Flag and V5-ubiquitin plasmids for 48 hours, followed by immunoprecipitation with anti-Flag antibody. TEAD2 and TEAD4 expression and PARylation of TEADs were detected with anti-Myc antibody and anti-PAR antibody respectively (n=3). **(D)** TEAD ubiquitination is significantly reduced upon knock down of *PARP1*. HEK 293 cells were transfected with specific guide RNAs to transiently knock out *PARP1*. The control cell line and *PARP1* KO cell line were further transfected with TEAD4Myc and V5-ubiquitin plasmids for 48 hours, followed by immunoprecipitation with an anti-V5 antibody. TEAD4 expression and ubiquitinated TEAD4 were detected with anti-Myc antibody (n=3). **(E)** PARylation of TEAD is located in the DNA binding domain (Asp70 site on TEAD4). Structure of TEAD4 DNA binding domain in complex with DNA (Shi et al., 2017) with labeled sites for PARylation (green) and ubiquitination (magenta). **(F)** TEAD4(D70A) mutation affects PARylation. HEK 293 cells were

transfected with duo tagged TEAD-Myc-Flag and V5-ubiquitin plasmids for 48 hours, followed by immunoprecipitation with anti-Flag antibody. TEAD2, TEAD4 and TEAD4(D70A) expression and PARylation of TEADs were detected with anti-Myc antibody and anti-PAR antibody respectively (n=2). **(G)** The ubiquitination of TEAD is significantly reduced in the absence of PARylation. HEK293 cells were transfected with TEAD4-Myc or TEAD4(D70A)-Myc and V5-ubiquitin plasmids for 48 hours, followed by immunoprecipitation with an anti-V5 antibody. TEADs expression and ubiquitinated TEADs were detected with anti-Myc antibody (n=3).

Figure 4. Overexpression of RNF146 E3 ligase antagonizes the overgrowth phenotype caused by the Hpo mutant. **(A)** PARylation site for TEAD is conserved in humans and Drosophila melanogaster as shown in the alignment of TEAD1/2/3/4 and Sd protein sequences. **(B, C)** Overexpression of RNF146 can rescue the overgrowth phenotype caused by hpo RNAi. In B, the first panel represents the expression of a control RNAi (ey:: Gal4>UAS:: luciferase RNAi) (n=9). The second panel represents knockdown of Hpo (w1118; ey::Gal4/+: UAS::hpoRNAi/+), which results in a significantly larger eye compared to luciferase RNAi control (n=10). The third panel represents overexpression of RNF146 (ey::Gal4>UAS::RNF146) (n=9). In the fourth panel, overexpression of RNF146 in a hyperactive Yki background (hpo RNAi) rescues the over-growth phenotype resulting in a significantly smaller eye (n=13). C is the quantification of B. Means +/- S.D. of eye area quantified per genotype are shown in arbitrary units (A.U.). One-way ANOVA with Sidak's multiple comparisons. Numbers (n) of eye area quantified and P-values are indicated above. **(D, E)** Overexpression of RNF146 can rescue the over-growth phenotype caused by Hpo loss of function mutation. (D) Wild-type control clones were generated using the eyFLP system (genotype: w1118; neoFRT42D, +/neoFRT42D, GMRHid; ey::Gal4, UAS::FLP/+) (Newsome et al., 2000) (n=11, both eyes). hpo^{KC202} mutant clones (genotype: w^{1118}; FRT42D, hpoKC202/FRT42D, GMRHid; ey::Gal4,UAS::FLP/+) result in a large, folded eye with cuticle overgrowth around the eye. This increase in eye area was significant compared to eyes of WT clones. ($p<0.0001$; n=9, both eyes). Clones overexpressing RNF146 showed no phenotype compared to control (genotype: w^{1118}; FRT42D, + /FRT42D, GMRHid; *ey*Gal4, UAS::FLP/UAS::RNF146^{OE}; n=11, both eyes). Combining hpo^{KC202} and RNF146 overexpression (genotype: w^{1118}; FRT42D, hpoKC202/FRT42D, GMRHid; ey::Gal4,UAS::FLP/ UAS::RNF146^{OE}) resulted in a significantly smaller eye as compared to the hpo^{KC202} mutant only. ($p=0.0027$; n=6, both eyes). E is the quantification of eye area of all of the eyes in D. Means +/- S.D. of eye area quantified per genotype are shown in arbitrary units (A.U.). One-

way ANOVA with Sidak's multiple comparisons. Numbers (n) of eye areas quantified and P-values are indicated above.

Figure 5. *TEAD* knockdown induces robust Hippo pathway suppression. **(A)** Cell viability assessed by Cell Titer-Glo upon siRNA treatment of *TEAD1-4* in Hippo/TEAD sensitive (NF2null/YAP1 amplified) and insensitive cell lines (no YAP1/WWTR1). Cells were treated with siNTC (dark gray bars), siTox (light gray bars) and siTEAD1-4 (red bars) for 72hr before cell viability assay. **(B)** Tumor growth (measured as tumor volume) in xenograft mice upon *TEAD1-4* knockdown in MDA-MB-231cells in presence of sucrose (red) and doxycycline (green). shNTC is control non-targeting shRNA (black and blue). **(C)** Chemical structures, biochemical data and cellular activity of all CIDEs screened. **(D)** Crystal structure of compound A bound to TEAD. **(E)** Protein abundance measurements made using tandem mass tag quantitative mass spectrometry and plotted as a log fold change. The scatterplot depicts the change in relative protein abundance inMDA-MB-231 cells when treated with compound D (x-axis) and compound E (y-axis) relative to protein abundance in compound A treated cells. Cells were treated with 0.5mM of compound for 8 hours before harvesting.

Figure 6. CIDEs mediated TEAD degradation is dependent on CRBN and the ubiquitin-proteasome pathway (A) Immunoblot for pan-TEAD, PDE6δ, YAP, TAZ and β-Actin in MDA-MB-231 after 24h of compound D treatment at the indicated concentrations (0.128, 0.8, 5 μM). **(B)** Immunoblot for pan-TEAD, YAP, TAZ and β-Actin in OVCAR-8 after 16h treatment of compound A/compound E/compound D at the indicated concentrations of 0.1μM, 1μM and 10 μM. **(C)** Immunoblot for pan-TEAD, YAP, TAZ and β-Actin in OVCAR8 upon co-treatment with DMSO/ compound E /compound D (1 μM) for 5 hours and MG132 (10 μM) for 6 hours. **(D)** Immunoblot for pan-TEAD, YAP, TAZ and b -Actin in MDA-MB-231 cells upon co-treatment with DMSO/ compound D/ compound E (1 μM) for 5 hours and MLN-7243 (1 μM) for 6 hours. **(E)** Immunoblot for pan-TEAD, YAP, TAZ and β-Actin in MDA-MB-231 cells upon treatment with DMSO/compound E/compound D (0.1 μM and 0.5 μM) for 16 hours in siRNA (CRBN and control) treated cells. siRNA treatment was done for 3 days followed by degrader treatment.

Figure 7. TEAD degradation inhibits cell proliferation and downstream Hippo pathway signaling. (A, B) Cell viability assessed using CellTiter-Glo in (A) OVCAR-8, (B) SK-N-FI after 6 days of treatment with compound D (red), compound E (green), compound A (purple), compound B (blue) and DMSO (black). Error bars represent the standard deviation of five technical replicates. **(C, D)** Crystal violet growth assay in OVCAR-8 (Hippo dependent) and SK-N-FI (Hippo independent) after 6 d treatment with compound D at indicated concentrations. **(E, F)** RNA-seq of Hippo signature genes after compound D/compound A treatment in MDA-MB-231 cell line. Hippo signature genes exhibit significant downregulation upon treatment with compound D in a concentration dependent manner. Cells were treated with 0.1 µM and 0.5 µM of compoundA/D for 24 hours before harvesting.

Figure 8. Compound D specifically reduces chromatin accessibility at TEAD motifs. (A) Differential analysis of ATAC-seq of OVCAR-8 cells treated with DMSO or Compound D for 48 hours performed by DiffBind. **(B)** Genomic annotations of the differential ATAC-seq peaks by ChIP-Annotate **(C)** UCSC browser view of ATAC-seq at known targets of TEAD, ANKRD1 and CCN1. **(D)** Lost ATAC-seq peaks were visualized by Deeptools and analyzed for motif enrichment by HOMER. **(E)** Lost peaks were assigned to genes using known distal enhancer-gene target links in Poly-Enrich and the 10 most significant pathways are shown.

SUPPLEMENTARY FIGURE LEGENDS

Figure S1: (A) Structure of TEAD4 DNA binding domain in complex with DNA) (Shi et al., 2017). All predicted TEAD4 lysine ubiquitination sites that were identified from the LC-MS/MS in figure 1 are labeled in magenta in the structures. **(B)** Structure of TEAD4 YAP-binding domain (blue) in complex with YAP1 (green) (Mesrouze et al., 2017). All predicted lysine ubiquitination sites are labeled in magenta. **(C)** Geyser plots showing changes in ratio and significance of ubiquitination of the whole proteome under MG132 treatment vs. DMSO. TEAD4 was highlighted by red dots and annotated.

Figure S2: (A, B) Validations of the E3 ligase screen. In A, a sub-list of candidate siRNAs (2 siRNA for each target) was identified from the siRNA libraries of Figure 2. MCF-7 cell line carried TEAD reporter were transfected with siRNAs for 72 hours in a 96 well-plate format (n=3). The signal was normalized to the negative control which is set at 100.

In B, the same transfection was done as in A, followed by Taq-man assay for Hippo target genes. **(C)** TEAD ubiquitination is reduced upon knockdown of *RNF146*. To transiently knockout RNF146, HEK293 cell line was transfected with sgRNF146 for 48 hours. TEADs-Myc and V5-ubiquitin plasmids were then transfected for an additional 48 hours and an *in vivo* ubiquitination assay was performed as described in Figure 1. TEADs expression and ubiquitinated TEADs were detected with anti-Myc antibody. β-Actin served as a loading control (n=3). **(D, E)** OVCAR-8 cells were transfected with siRNAs for *RNF146*, *YAP1* as indicated for 48hrs. RNA-seq was performed to measure *YAP1* and *RNF146* level as control. **(F)** Taq-man analysis showing upregulation of Hippo signature gene expression upon *RNF146* knockdown in human cancer cell lines. Cells were treated with siNTC (dark gray bars), si*YAP1* (red bars) and si*RNF146* (green bars) for 72hr before harvesting for Taq-man RT-qPCR. **(G)** RNF146 knockdown enhanced TEAD4 half-life, which is rescued by MG132 treatment. OVCAR-8 cells were treated with si*RNF146* for 48 hours. Note that 100 μg/mL of CHX or 10 μM of MG132 was added as a time course before cell harvest. Expression of indicated proteins was assessed by immunoblotting. β-Actin served as a loading control. **(H-I)** RNF146 knockdown enhanced TEAD4 half-life. H226, PATU-8902, Detroit-562, OVCAR-8 cells were treated with si*RNF146* (H) or sgRNF146 (I). Note that 100 μg/mL of CHX was added for 15hrs before cell harvest. Expression of indicated proteins was assessed by immunoblotting. Levels TEAD4 protein were compared at 15hrs post ChX added. ** indicated t-test with p-value ≤ 0.05 (n=3). Quantification of protein level was done and normalized to siNTC (no ChX). β-Actin served as a loading control.

Figure S3: (A, B) RNF146 protein can be detected in nuclear and cytoplasmic of the cell. Detroit-562 cells were stained with RNF146 and NUP98 antibodies as well as DAPI. Pan-TEAD and YAP were used as controls. (n=3). In B, Detroit-562 and Patu-8902 were fractionated for nuclear and cytoplasmic compartments. Immunoblotting was performed with the RNF146 antibody as well as other members of the Hippo pathway were probed respectively. **(C)** The schematic diagram for the PLA assay performed in Figure 2D using TEAD4 antibodies that can detect both isoforms of TEAD4. The PLA signals in Figure 2D were mostly found in the nucleus. **(D)** RNF146 interacts with full-length TEAD4. PLA was performed using an anti-TEAD4 antibody (raised in mouse) and anti-RNF146 antibody (raised in rabbit) for detecting endogenous proteins, followed by imaging with confocal microscopy as described in the

method section. Arrows indicate the foci of interaction (n=8). **(E)** The ubiquitination of TEAD is significantly reduced upon knockdown of *PARP1*. HEK293 cells were transfected with specific siRNAs to knockdown *PARP1*. The cell lines were further transfected with TEADs-Myc and V5-ubiquitin plasmids for 48 hours, followed by immunoprecipitation with an anti-V5 antibody. TEAD4 expression and ubiquitinated TEADs were detected with anti-Myc antibody (n=3). **(F)** D70A mutation enhanced TEAD4 half-life. MDA-MB-231 with shTEAD1-4, Dox inducible cells were treated with Dox for 24 hours to deplete endogenous TEADs, followed by transfection of TEAD4-Flag-Myc and TEAD4(D70A)-Flag-Myc and si*RNF146* treatment for 48 hours. Note that 100 µg/mL of CHX or 10 µM of MG132 was added as a time course before cell harvest. Expression of indicated proteins was assessed by immunoblotting. β-Actin served as a loading control.

Figure S4: (A, B) Knockdown of Scalloped results in a significantly small eye phenotype. In A, the first panel represents a control RNAi (ey:: Gal4>UAS:: luciferase RNAi) using an eye-specific driver (n=10). The second panel represents knockdown of Hpo (w1118; ey::Gal4/+: UAS::hpoRNAi/+), which results in a significantly larger eye compared to luciferase RNAi control. (n=10). The third panel represents RNAi of Sd (ey:: Gal4>UAS:: SdRNAi), which results in a significantly smaller eye phenotype compared to luciferase RNAi control. (n=9). The fourth panel represents RNAi of Sd in a hyperactive Yki background (hpoRNAi). It displays a similar phenotype of the RNAi of Sd with a significantly smaller eye (n=10). Means +/- S.D. of eye area quantified per genotype are shown in arbitrary units (A.U.) in B. One-way ANOVA with Sidak's multiple comparisons. Numbers (n) of eye area quantified and P-values are indicated above. **(C, D)** RNAi of RNF146 enhances the over-growth phenotype caused by hpo RNAi. In C, the first panel represents a control RNAi (ey:: Gal4>UAS:: luciferase RNAi) using an eye-specific driver (n=7). The second panel shows knockdown of Hpo (w1118; ey::Gal4/+: UAS::hpoRNAi/+) results in a significantly larger eye compared to luciferase RNAi control. Also, the folding of the cuticle is seen behind the eye (n=10). The third panel represents eyes RNAi of RNF146 (ey:: Gal4>UAS:: RNF146RNAi) (n=10). In the fourth panel, RNAi of RNF146 in a hyperactive Yki background (hpoRNAi) did not rescue the overgrowth phenotype and displayed an additive phenotype with a much larger eye (n=13). D shows the quantification of C in comparing to Figure 4B and C. Means +/- S.D. of eye area quantified per genotype are shown in arbitrary units (A.U.). One-way ANOVA with Sidak's multiple comparisons. Numbers (n) of eye area quantified and P-values are indicated above. **(E)** Overexpression of Sd displays a dominant-negative phenotype.

However, the overexpression of RNF146 does not rescue this phenotype. In the first panel, a control RNAi (ey:: Gal4>UAS:: luciferase RNAi) does not have a visible phenotype. (n=9). Second panel represents overexpression of RNF146 (ey::Gal4>UAS::RNF146) (n=9). The third panel represents the overexpression of Sd (ey:: Gal4>UAS:: Sd/+) results in a dominant-negative phenotype. (n=7). The fourth panel represents the overexpression of RNF146 in a dominant-negative background of Sd overexpression. RNF146 overexpression did not rescue the phenotype of Sd overexpression, resulting in significantly smaller eyes and non-viable flies. The combination is very detrimental to the flies and we could not collect enough flies for data quantification.

Figure S5: (A) Taq-man analysis showing downregulation of TEAD1-4 and Hippo signature gene *CTGF* mRNA expression upon *TEAD1-4* knockdown in human cancer cell lines. Cells were treated with siNTC (dark gray bars), and siTEAD1-4 (red bars) for 72hr before harvesting for Taq-man. **(B)** Immunoblot analysis of NF2, pan-TEAD, YAP, TAZ and β-actin upon *TEAD1-4* knockdown in Hippo pathway insensitive cell lines. **(C)** Weight change in xenograft mice upon *TEAD1-4* knockdown in MDA-MB-231 in presence of sucrose (red) and doxycycline (green). shNTC is control non-targeting shRNA (black and blue). **(D)** Taq-man analysis confirming knockdown of *TEAD 1-4* in engineered MDA-MB-231 cell line used for the xenograft study. **(E)** Chemical structure and biochemical data of TEAD-CIDEs screened in the study. **(F)** Abundance of different peptides identified with compound D, compound E and compound A as a function of time in proteomics analysis. Cells were treated with 0.5mM of compound for 0, 2h, 4h and 8h.

Figure S6: (A) Immunoblot of pan-TEAD, YAP, TAZ and β-Actin as a function of time (0, 30min, 2h, 4h, 8h, 24h) upon compound D, compound E and compound A treatment in MDA-MB-231 cells. **(B)** Immunoblot of pan-TEAD, YAP, TAZ and b-Actin upon compound B treatment in OVCAR8 cells for 16 hours. **(C)** Docked structure of PDE6δ with compound A in the PDE6δ structure (PDB 5ML2) compound A in cyan, native PDB ligand (for comparison) in magenta. **(D, E)** PDE6δ dependency from Achilles data measured as CERES score shows no correlation with CERES scores of *WWTR1* and *NF2*.

Figure S7: (A) Cell viability data from 3D Cell Titer -Glo assay (in Relative luciferase unit) of Hippo/TEAD sensitive cell lines (in blue), black is DMSO control treated cells **(B)** Cell viability data from 3D Cell Titer -Glo assay (in Relative luciferase unit) of Hippo/TEAD insensitive cell lines (in blue), black is DMSO control treated cells. SK-N-FI curve is shown in red.

SUPPLEMENTARY TABLE LEGENDS

Supplementary Table 1: KGG peptide counts for TEAD4

Supplementary Table 2: Ubiquitin linkages in TEAD IP mass-spec of Patu-8902

Supplementary Table 3: siRNA screen to identify negative regulators for the luciferase reporters driven by multimerized TEAD binding sites (8xGTIIC-Luc)

Supplementary Table 4: IP mass-spec in Patu-8902

Supplementary Table 5: X-ray crystallography data collection and refinement statistics

MATERIALS and METHODS

Cell lines, antibodies, and other reagents

Cell lines used in this study are HEK293T, Detroit 562, OVCAR-8, PATU-8902, MDA-MB-231, HCC1576, NCI-H226, MS751, NCI-H2373, SNU-423, HCSC-1 and SK-N-FI which were obtained from American Type Culture Collection (ATCC). MCF-7a TEAD-Luc was purchased from BPS Bioscience. Cell line authentication was conducted for Short Tandem Repeat (STR) Profiling using the Promega PowerPlex 16 System. This process was performed once when receiving a new cell line and compared to external STR profiles of cell lines (when available) to determine cell line ancestry. Routine authentication was conducted by SNP-based genotyping using Fluidigm multiplexed assays at the Genentech cell line core facility.

Antibodies used in this study are pan-TEAD (13295, CST); YAP(14074, CST); TAZ (70148, CST); MAX (sc-765 and sc-8011, Santa Cruz); α-Tubulin (3873, CST); β-Actin (3700, CST); cleaved PARP (9541, CST); FRA1(5281, CST); Myc-tag (2278-CST); V5 (680602, Biolegend); RNF146 (HPA027209, Sigma-Aldrich); TEAD4 (Abcam 58310); PARP1 (9532, CST); NUP98 (50610, Abcam); DAPI (4083, CST); CRBN (11435-1-AP, Proteintech); Anti-rabbit and anti-mouse HRP linked (7074 and 7076, CST), IRDye anti-rabbit and anti-mouse (68070 and 32211, Li-cor). siRNAs were purchased from Dharmacon, including siNTC (D-001810-10), si*RNF146* (L-007080-00), si*PARP1* (L-006656-03). MG132 solution (M7449) was from Sigma-Aldrich. MLN7243 was purchased from Selleckchem. On target plus Human CRBN siRNAs (51185) and non-targeting siRNA pool were purchased from Horizon Discovery.

***In-vivo* ubiquitination assay**

Myc-Flag-human TEADs (OriGene) and V5-ubiquitin (generated in house) plasmids were transfected into HEK293T cells at a ratio of 3:1 with Lipofectamine 3000 (Thermo Fisher Scientific). After 48 hours, cells were lysed in NP-40 buffer (1% NP-40, 120 mM NaCl, 50 mM Tris, pH 7.4, 1 mM EDTA, pH 7.4, 20mM cysteine protease inhibitor N-ethylmaleimide (NEM), protease and phosphatase inhibitors (Roche). Proteins were denatured with 1% SDS at 94°C for 10 mins and then diluted to 0.05% SDS before anti-V5 immunoprecipitation. Immunoprecipitation was at 4°C on a turning rotor for overnight. After washing with NP-40 buffer and PBS, ubiquitination proteins were then detected by immunoblotting.

Immunoprecipitation and immunoblotting

Cells were lysed in RIPA lysis buffer (89900, Thermo Fisher Scientific) containing protease inhibitor (Roche), and phosphatase inhibitor (Roche). Lysates were prepared by taking supernatants from centrifugation at 12,000 g for 15 min at 4°C. Equivalent amounts of proteins were loaded and separated by SDS-PAGE followed by transferring to membranes.

For endogenous co-immunoprecipitation experiments, 1×10^7 cells were lysed using RIPA buffer and immunoprecipitation with indicated antibody overnight at 4°C. After washing with RIPA buffer, co-immunoprecipitated endogenous proteins were then detected by immunoblotting.

Subcellular Fractionation

Cells grown on 10 cm dishes (80% confluence) were harvested after washing with cold PBS. Cell pellets were then incubated with 200 µl of Buffer A [10 mM HEPES pH 7.9, 10 mM KCl, 1 mM EDTA, 0.1 mM EGTA, 0.2% NP-40, 10% glycerol, complete-mini (EDTA free) protease inhibitor (Roche), PHOStop phosphatase inhibitor (Roche) at 4°C for 20 min. Cytoplasmic fractions were collected by taking the supernatant after centrifugation for 5 minutes at 2500 × g. For the preparation of nuclear fraction, the pellets were then incubated with 50 µl of RIPA buffer (89900, Thermo Fisher Scientific) containing protease and phosphatase (Roche) for 30 min at 4°C. After centrifugation for 12 mins at 16,000 × g, nuclear fractions were collected by retaining the supernatant.

siRNA Screening

siRNA screening was performed in MCF-7 TEAD reporter cells using two different siRNA libraries (Dharmacon On-Target Plus and Ambion Silencer Select) targeting ubiquitin-related genes. The Dharmacon library comprised 4 siRNAs per gene, whereas as the Ambion had 3 per gene. Screening was conducted in biological replicate. Briefly, 2 pmol of siRNA (20 nM final concentration) was spotted to 384 well plates, and 0.08 µL Lipofectamine RNAiMax was added in 20 µL of serum-free EMEM media. This complex was incubated at ambient temperature for 30 minutes before adding 2,000 MCF-7 TEAD reporter cells in 20 µL of 20% serum EMEM media. Cells were incubated for 72 h before assaying by OneGlo luciferase assay reagent (Promega). All plates included 8 wells of negative control siRNA (Ambion Silencer Select Negative Control #2), 8 wells of cell death control (Qiagen AllStars Positive Control siRNA), and 8 wells of YAP targeting siRNA (Ambion Silencer Select, cat# s20366). Positive controls were used to gauge transfection efficiency and yielded assay z' factors of 0.5 and 0.3 respectively. After normalization of sample wells to negative control siRNA on each plate, robust z-scores (Chung et al., 2008) were calculated. Replicate values were averaged and gene-level p-values were calculated using RSA (König et al., 2007). Parallel screens were also used to assess effects on viability. All data can be found in Supplemental Table 2. All seven siRNAs tested against RNF146 yielded a significant increase in reporter activity (Fig 2A).

siRNA transfection

Cells were seeded at 15000/well on a 6-well plate for 24 hours. The following day, cells were treated with the siRNAs (final concentration 20nM) using Lipofectamine RNAi Max in serum free RPMI media for 72 hours before collection. siRNAs were purchased from Dharmacon, including siNTC (D-001810-10), si*TEAD1* (J-012603-05), si*TEAD2* (J-012611-09), si*TEAD3* (L-012604-00), siT*EAD4* (J-019570-09), si*RNF146* (L-007080-00), si*PARP1* (L-006656-03), si*CRBN* (51185). Knockdown was confirmed by Western blot with the following antibodies from Cell Signaling Technology: pan-TEAD (13295, CST); YAP (14074, CST); TAZ (70148, CST); β-Actin (3700, CST).

RNA extraction, cDNA synthesis and quantitative RT-PCR

Tumors and cell lines were dissociated and lysed for RNA isolation using RNAeasy kit (Qiagen). cDNA was prepared by reverse transcription using the iScript cDNA synthesis Kit (Bio-Rad) as the manufacture's protocol. The quantitative RT-PCR was performed using QuantStudio 7 Flex machine with TaqMan probes for *TEAD1* (Hs00173359_m1), *TEAD2* (Hs01055894_m1), *TEAD3* (Hs00243231_m1), *TEAD4* (Hs01125032_m1), *RNF146* (Hs00258475_s1), CTGF (Hs00170014_m1) and *GAPDH* (Hs02786624_g1) (Applied Biosystems). Relative expression of each gene to *GAPDH* of target genes was assessed for at least 3 biological replicates.

In situ PLA

In situ PLA was performed with Duo-link in situ reagents (Sigma) following the instructions from the product manual. Primary antibodies used in PLA were anti-TEAD4 antibody (Abcam 58310); RNF146 (HPA027209, Sigma-Aldrich); YAP (14074, CST); DAPI (4083, CST). Images were acquired with a Leica TCS SP5 confocal microscopy equipped with a CCD camera.

KGG ubiquitination site detection

PTMScan® analysis: Cells were harvested and lysed in 20 mM HEPES pH 8.0, containing 9 M urea, 1 mM sodium orthovanadate, 2.5mM sodium pyrophosphate, and 1mM β-glycerophosphate. Whole-cell lysates from 4 conditions, control & overexpressed TEAD4 -/+ MG132 treatment (35 mg/condition) were subjected to reduction with 5 mM dithiothreitol (DTT) at 37 °C for 1h followed by alkylation with 10 mM iodoacetamide (IAA) in the dark at RT for 15 min. The protein mixture was diluted with HEPES buffer such that the final concentration of urea was 2M.

Tryptic digestion was performed at an enzyme: substrate ratio of 1:50 at 37 ˚C overnight. After incubation, the digestion was quenched with 20% trifluoroacetic acid (TFA) and excipients were removed from the peptide mixture using C18 Sep-pak® column (Waters, Milford, MA). Peptides were eluted with 3 x 4 mL of 40% acetonitrile (ACN)/0.1% TFA. The eluent was lyophilized to complete dryness. Immuno-affinity isolation of peptides containing di-glycine remnant (-GG) on lysine residues was performed using antibody recognizing the KGG motif according to the PTMScan® protocol (Kim et al., 2011; Rush et al., 2005). PTMScan® Proteomics System was in-licensed from Cell Signaling Technologies (Danver, MA). http://www.cellsignal.com/services/peruse_licensing.html

Mass spectrometric analysis: Samples were reconstituted in solvent A (2% ACN/0.1% formic acid (FA)), and injected via an auto-sampler for separation by reverse phase chromatography on a NanoAcquity UPLC system (Waters, Dublin, CA). Peptides were loaded onto a Symmetry® C18 column (1.7 mm BEH-130, 0.1 x 100 mm, Waters, Dublin, CA) with a flow rate of 1 µL/minute and a gradient of 2% to 25% Solvent B (where Solvent A is 0.1% Formic acid (FA)/2% acetonitrile (ACN)/water and Solvent B is 0.1% FA/2% water/ACN) applied over 85 minutes, with a total analysis time of 120 minutes. Duplicate injections were made. Peptides were eluted directly into an Advance CaptiveSpray ionization source (Michrom BioResources/Bruker, Auburn, CA) with a spray voltage of 1.4 kV and were analyzed using a Q Exactive-HF mass spectrometer (ThermoFisher, San Jose, CA). Precursor ions were analyzed in the Orbitrap at 60,000 resolution; MS/MS data were acquired at 15,000 resolution. The instrument was operated in data-dependent mode whereby the top 10 most abundant ions were subjected for HCD fragmentation.

Bioinformatic data analysis: MS/MS spectra were searched using the search algorithm Mascot (Matrix Sciences, London, UK) against a concatenated target-decoy database (UniProtKBConcat 2016_06) comprised of the UniProt human protein sequences, known contaminants and the reversed versions of each sequence. A 50 ppm precursor ion mass tolerance and 0.05 Da fragment ion tolerance were selected with tryptic specificity, up to 3 miscleavages were allowed. Variable modifications were permitted for methionine oxidation (+15.9949 Da), iodoacetamide adduct for cysteine residues (+57.0215 Da), and ubiquitin di-glycine remnant (-GG signature) on lysine residues (+114.0429 Da). Peptide assignments were first filtered to a 5% false discovery rate (FDR) at the peptide level followed by filtering at the protein level at 2 % FDR. The AScore algorithm was applied on a subset of peptides

containing ubiquitinated species for site localization. Label-free quantitation of the KGG peptides across all four conditions was performed using XQuant, an algorithm that utilizes retention times to quantify peptides across runs (Bakalarski et al., 2008; Kirkpatrick et al., 2013). Linear mixed-effect modeling was performed for each protein to summarize peptide level changes. Significance values were calculated from the model, which considered replicate peptide measurements and repeat injections (Yu et al., 2015).

Project Achilles data analysis

Genome-wide CRISPR KO data (20Q1) was downloaded from depmap.org/portal/download. Univariate linear regressions were performed for all pairwise gene comparisons for 739 cancer cell lines. Gene-gene pairs with p-value $< 10^{-20}$ were considered for visualization. Graph network included genes within 2 degrees of separation to WWTR1 (TAZ) were visualized using igraph v. 1.2.5 R package. Communities were identified using random walks on graph network.

Fly Lines and Husbandry

Flies were cultured on yeast/molasses-based food at 25°C or 29°C at 60% humidity with a 12-hr light/dark cycle. Female or male flies were used in all experiments. The following stocks were obtained from the Bloomington Stock Center (University of Indiana, Bloomington, IN): ey-gal4 (BL5535); luciferase TRiP RNAi (BL31603); y[d2] w[1118] P{ry[+t7.2]=ey-FLP.N}2; P{ry[+t7.2]=neoFRT}42D hpo[KC202]/CyO, P{w[+mC]=GAL4-Kr.C}DC3, P{w[+mC]=UAS-GFP.S65T}DC7 (BL25090); y[1] w[*]; P{ry[+t7.2]=neoFRT}42D P{y[+t7.7] ry[+t7.2]=Car20y}44B, P{w[+mC]=GMR-hid}SS2, l(2)CL-R[1]/CyO; P{w[+m*]=GAL4-ey.H}SS5, P{w[+mC]=UAS-FLP.D}JD2 (BL5251); P{ry[+t7.2]=neoFRT}42D; ry[605] (BL1802). The Hpo knockdown line was obtained from Vienna Drosophila Stock Center (Vienna Biocenter Core Facilities, Vienna, Austria) w1118; P{GD14028}v36028 (VDRC104169). The RNF146 overexpression line was obtained from FlyORF Zurich ORFeome Project (University of Zurich) M{UAS-RNF146.ORF.3xHA}ZH-86Fb (F003712). Recombinant lines ey-gal4 + UAS::hpoRNAi (BL5535 and VDRC104169) were generated using standard genetic methods.

Eye Imaging

Fly eye imaging was done using a LEICA M205FA stereoscope with the LEICA DFC 7000T camera. The light source used was a LEICA KL 1500 LCD fiber optic ring light. Flies were frozen at -80°C for two hours, heads were removed, and oriented using an apple agar plate.

Image and Statistical Analysis

The eye area (A.U.) was obtained using ImageJ by drawing an ROI around the eye. For sample size per genotype see figure legend. One-way ANOVA with Sidak's multiple comparison test was performed using PRISM (GraphPad PRISM 7). Because of the variance between both eye sizes of the same fly, we measured each eye individually. Statistical analysis was performed using data of all eyes of multiple individual animals.

TEAD Lipid Pocket TR-FRET Assay

His-tagged TEAD proteins were pre-incubated with TEAD project compounds for 30 minutes at room temperature. Biotinylated lipid pocket probes are then added to the TEAD/Compound mixture and incubated for 60 minutes at room temperature. The lipid pocket probe competes with the test compound for the TEAD lipid pocket until equilibrium is reached. After 60 minutes, Europium labelled anti-His (Perkin Elmer # AD0110) and XL665 labelled streptavidin (CIS Bio 610SAXAC) are added to the TEAD/test compound/lipid pocket mixture and incubated for 30 minutes. TR-FRET values are then measured using an EnVision multi-label plate reader (Perkin Elmer Cat# 2104-0010A.) If the lipid pocket probe binds to TEAD as expected, a TR-FRET signal results from the proximity of anti-His Eu and XL665. If a TEAD lipid pocket binder such as binds and displaces the lipid pocket probe, the disruption of the TEAD:probe interaction results in a decrease in TR-FRET signal. The potency of compounds as TEAD lipid pocket binders is determined by IC50 value generated using a non-linear 4 parameter curve fit.

Docking Calculations

Compound compound A was docked to PDE6δ using the Schrodinger Software Suite 2019-4 (Schrödinger, 2019). The protein structure (PDB ID: 5ML2) was prepared for docking using the protein preparation wizard in the Maestro program. Water molecules were removed from the structure, and missing sidechain atoms for residues B10 and B26 were added using the preprocess module. The structure was optimized and minimized using default

parameters. Docking was performed using the Glide program. The Glide docking grid was constructed in Maestro's Receptor Grid Generation Module, and default parameters were used with the following two exceptions: (1) a van der Waals scaling factor of 0.8 was applied to the non-polar protein atoms to account for limited receptor flexibility and (2) a positional constraint was created to require docked ligands to have an atom located within 1 Å of the position of the chlorine atom in the 5ML2 structure ligand (the TEAD lipid pocket ligands often contain halogenated hydrophobic groups that are likely to bind in a similar position to the 5ML2 ligand chlorophenyl group). Poses from the docking calculations were analyzed for strain energy using the sdfMMConfAnalysis module of the Chemalot software package (Lee et al., 2017). The pose chosen from the docking study had the best combination of docking score and strain energy.

Cell viability assay

Cells were seeded at 500-1000/well on a 96-well plate for 24 hours. They were then treated with indicated siRNAs (final concentration of 25nM) or indicated inhibitors (with indicated concentration). Cell growth was assessed using CellTiter-Glo Luminescent Cell Viability Assay (Promega). All cell viability data was collected on an Envision luminescence microplate reader and calculated for at least 6 replicates per time point, per condition. IC_{50} for the inhibitors was determined by fitting the nonlinear regression curve generated by GraphPad Prism.

Crystal violet cell growth assays

Cells were seeded at 0.2 million cells per well in triplicate in 6 well plates for 24 hours. Cells were then treated with compounds at indicated concentration and grown for 6 days. Following, cells were washed in PBS, fixed in methanol for 10 min, stained with 0.5% crystal violet for 30 min, washed with water and air dried. Stained colonies comprising more than 30 cells were imaged using scanner.

***In-vivo* mouse xenograft study**

All mouse experiments were performed according to the animal use guidelines of Genentech, a Member of the Roche Group, conforming to California state legal and ethical practices. MDA-MB-231 shNTC or MDA-MB-231 shTEAD1-4, 10 million cells was implanted, with Matrigel, subcutaneously in the right flank region of female C.B-17

SCID.Bg (Charles River Laboratories) mice (n=35 each cell line; n=70 total). Mice were randomly assigned 10 mice per group when tumor volumes reached approximately 150 to 350 mm^3. The mice were stratified into four groups (n=10/group) for treatment as following: Group 1: MDA-MB-231 shNTC, 5% sucrose water; Group 2: MDA-MB-231 shNTC, 1 mg/ml Doxycycline; Group 3: MDA-MB-231 shTEAD1-4, 5% sucrose water; Group 4: MDA-MB-231 shTEAD1-4, 1 mg/ml Doxycycline. All water bottles were changed once (sucrose) or thrice (DOX) weekly. Tumor sizes and body weights were recorded twice weekly over the course of the study. Mice with tumor volumes ≥2000 mm^3 or recorded body weight loss ≥20% from were promptly euthanized. An MTD was defined as the dose in which <20% body weight loss or no animal deaths were observed. Tumor volumes were determined using digital calipers (Fred V. Fowler Company, Inc, Newton, MA) using the formula (L x W x W)/2. A generalized additive mixed model (GAMM) was then employed to analyze transformed tumor volumes over time (Liang, 2005; Lin and Zhang, 1999). All mice were euthanized by 34 days post first dose, unless earlier if needed due to mice reaching tumor, weight loss, or other humane endpoints. At end of study, tumors were collected after mice were euthanized for histopathological and in vitro analysis.

Protein Expression and Purification

TEAD2-YBD (A217-D447) was purified as described (Noland et al., 2016) with the exception that the proteins were treated with 2.5% hydroxylamine (Sigma) at pH 7.0 for one hour at room temperature prior to size exclusion chromatography. The final protein sample was concentrated to 5 mg/ml.

Crystallization

TEAD2-YBD crystals of the base-centered monoclinic space group *C*121 were grown at 19°C by hanging-drop vapor diffusion using a drop ratio of 1:1 protein:reservoir solution and streak seeding. Reservoir solution contained 200 mM Potassium/sodium tartrate pH 6.5 and 20% PEG 3350. To obtain co-crystal structures, crystals were soaked for five days in 2 μL reservoir solution containing a final concentration of 2 mM compound and 35% PEG 3350. Crystals were then flash-frozen directly in liquid nitrogen.

Data Collection and Structure Determination

X-ray diffraction data were collected at beamline 5.0.2 at the Advanced Light Source. Data were processed using autoPROC and elliptically truncated using STARANISO (Evans, 2006; Evans and Murshudov, 2013; Kabsch, 2010; Tickle, 2017; Vonrhein et al., 2011; Winn et al., 2011). All structures were solved by molecular replacement using Phaser (McCoy et al., 2007). There were two molecules in the asymmetric unit. Structures were rebuilt in Coot (Emsley and Cowtan, 2004) and subjected to iterative rounds of refinement and rebuilding using Phenix (Adams et al., 2010) and Coot. Data processing and refinement statistics are summarized in Supplemental Table 5.

RNA-seq and data analysis

Total RNA was extracted using the Qiagen RNAeasy kit with the on-column genomic DNA elimination.

RNA was quantified with Qubit RNA HS Assay Kit (Thermo Fisher Scientific) and quality was assessed using RNA ScreenTape on 4200 TapeStation (Agilent Technologies). For sequencing library generation, the Truseq Stranded mRNA kit (Illumina) was used with an input of 100 nanograms of total RNA. Libraries were quantified with Qubit dsDNA HS Assay Kit (Thermo Fisher Scientific) and the average library size was determined using D1000 ScreenTape on 4200 TapeStation (Agilent Technologies). Libraries were pooled and sequenced on NovaSeq 6000 (Illumina) to generate 30 millions of single-end 50-base pair reads for each sample.

For RNA-seq data analysis, RNA-seq reads were first aligned to ribosomal RNA sequences to remove ribosomal reads. The remaining reads were aligned to the human reference genome (GRCh38) using GSNAP version "2013-10-10," allowing a maximum of two mismatches per 75 base sequence (parameters: '-M 2 -n 10 -B 2 -i 1 -N 1 -w 200000 -E 1 --pairmax-rna=200000 --clip-overlap). Transcript annotation was based on the Ensembl genes database (release 77). To quantify gene expression levels, the number of reads mapped to the exons of each RefSeq gene was calculated.

Global proteome sample preparation

MDA-MB-231 cells were treated with DMSO and 0.5μM of compound A/D/E for 0, 2h, 4h, 8h. Cell pellets were lysed in 8 M urea, 150 mM NaCl, 50 mM HEPES (pH 7.2), and complete-mini (EDTA free) protease inhibitor (Roche) by 15X passages through a 21g needle. Protein concentrations were then estimated by BCA assay (ThermoFisher Pierce,

Rockford, IL). Disulfide bonds were reduced by incubation with 5 mM DTT (45 min, 37°C), followed by alkylation of cysteine residues by 15 mM IAA (30 min, RT Dark), and finally capped by the addition of 5 mM DTT (15 min, RT Dark). Proteins were then precipitated by chloroform/methanol precipitation and resuspended in digestion buffer (8 M urea, 150 mM NaCl, 50 mM HEPES pH 8.5). Initial protein digestion was performed by the addition of 1:100 LysC followed by incubation at 37°C for 3 hours. Samples were then diluted to 1.5 M urea with 50 mM HEPES (pH 8.5) before the addition of 1:50 Trypsin and incubation overnight at room temperature. Peptide mixtures were acidified and desalted via solid phase extraction (SPE; SepPak - Waters, Boston, MA).

Peptides were resuspended in 200 mM HEPES (pH 8.5) and a 100µg aliquot of peptides was mixed with tandem mass tags (TMT, ThermoFisher Pierce, Rockford, IL) at a label to protein ratio of 2:1. After 1 hour of labeling the reaction was quenched by the addition of 5% hydroxylamine and incubated at room temperature for 15 min. Labeled peptides were then mixed, acidified, and purified by SPE.

Labeled samples were separated by offline high pH reversed-phase fractionation using an ammonium formate based buffer system delivered by an 1100 HPLC system (Agilent). Peptides were separated over a 2.1x150 mm, 3.5 µm 300Extend-C18 Zorbax column (Agilent) and separated over a 75-minute gradient from 5% ACN to 85% ACN into 96 fractions. The fractions were concatenated into 24 samples of which 12 were analyzed for proteome quantification. Fractions were concatenated by mixing different parts of the gradient to produce samples that would be orthogonal to downstream low pH reversed phase LC-MS/MS. Combined fractions were dried, desalted by SPE, and dried again.

Quantitative mass spectrometry and data analysis

nanoLC-MS/MS analysis was performed on an Orbitrap Fusion Lumos mass spectrometer (ThermoFisher, San Jose, CA) coupled to a Waters NanoAcquity UPLC (Waters, Milford, MA). Peptides were separated over a 100 µm X 250 mm PicoFrit column (New Objective) packed with 1.7 µm BEH-130 C18 (Waters, Milford, MA) at a flow rate of 500 nL/min for a total run time of 180 min. The gradient spanned from 2% Buffer B (0.1% FA/98%ACN/2% water) to 30% B over 155 minutes and then to 50% B at 160 minutes. For mass spectrometry analysis peptides were surveyed within FTMS1 analyses (120,000 resolution, AGC = 1x106, maximum injection time [max IT] = 50 ms) and the top 10 peaks were selected for MS/MS ensuring that any given peak was only selected once in a 45 second window (ppm tolerance = 5 ppm). For dynamic exclusion the “one precursor per charge state” was ON. For MS2 analysis precursors

were isolated using the quadrupole (0.5 Th window), fragmented using CAD (NCE = 35, AGC = $1.5x10^4$, max IT = 100 ms), and analyzed in the ion trap (scan speed = Turbo). Following MS2 analysis, the top 8 ions were simultaneously selected (synchronous precursor selection – SPS, AGC = $1.5x10^5$, max IT = 150 ms) and fragmented by HCD (NCE=55) before analysis in the Orbitrap (resolution = 50,000). Raw data files are available via the MASSIVE data repository using the identifier MSV000085331.

All mass spectrometry data was searched using Mascot against a concatenated target-decoy human database (downloaded June 2016) containing common contaminant sequences. For the database search a precursor mass tolerance of 50 ppm, fragment ion tolerance of 0.8 Da, and up to 2 missed cleavages. Carbamidomethyl cysteine (+57.0214) and TMT labeled n-terminus and lysine (+229.1629) were applied as static modifications, while methionine oxidation (+15.9949) was set as a dynamic modification. Peptide spectral matches for each run were filtered using line discriminant analysis (LDA) to a false discovery rate (FDR) of 2% and subsequently as an aggregate to a protein level FDR of 2%. TMT-MS3 quantification was performed using Mojave, with only those PSMs possessing isolation specificities greater than or equal to 0.7 considered for the final dataset. Intensities of each PSM were added to the peptide and then protein (proteome) level within R. Expression is reported as relative abundance, which is the measured intensity of any given channel divided by the total intensity for that protein.

ATAC-seq analysis

ATAC-seq reads were analyzed using the ENCODE ATAC-seq pipeline v1. Briefly, reads were trimmed of adapters by cutadapt (version 1.9.1, cite DOI:10.14806/ej.17.1.200) and mapped to hg38 by Bowtie2 (version 2.2.6, cite https://doi.org/10.1038/nmeth.1923). Bam files were converted to tagAlign format which was then adjusted for Tn5 insertion sites by shifting +4bp for positive strand and by -5bp for negative strand. TagAlign files were used to call peaks using MACS2 (version 2.1.0, cite DOI: 10.1186/gb-2008-9-9-r137) and those peaks with p<1e-6 were retained for differential analysis by Diffbind (version 3.0.13, cite http://www.nature.com/nature/journal/v481/n7381/full/nature10730.html). Differential peaks were defined by absolute fold change > 1 and FDR < 0.01. Genomic distribution of differential peaks was annotated by ChIPpeakAnno (version 3.24.1, cite doi: 10.1186/1471-2105-11-237). Bigwigs corresponding to fold change against the background control were generated by MACS2 and used to generate heatmaps by the pheatmap function of Deeptools (version

3.5.0, cite doi:10.1093/nar/gkw257). Motif analysis of differential peaks was performed using HOMER (version 4.10) with all peaks as the background. The peaks were assigned using Poly-Enrich (cite https://doi.org/10.1093/nargab/lqaa006) with distal enhancer-gene target links (>5kb from TSS) plus 5kb locus definitions. Gene set enrichment was searched against Gene Ontology, MsigDB Oncogenic and Hallmark.

References

Adams, P. D., Afonine, P. V., Bunkóczi, G., Chen, V. B., Davis, I. W., Echols, N., Headd, J. J., Hung, L.-W., Kapral, G. J., Grosse-Kunstleve, R. W.*, et al.* (2010). PHENIX: a comprehensive Python-based system for macromolecular structure solution. Acta crystallographica Section D, Biological crystallography *66*, 213-221.

Bakalarski, C. E., Elias, J. E., Villén, J., Haas, W., Gerber, S. A., Everley, P. A., and Gygi, S. P. (2008). The Impact of Peptide Abundance and Dynamic Range on Stable-Isotope-Based Quantitative Proteomic Analyses. Journal of Proteome Research *7*, 4756-4765.

Butler, A. J., and Ordahl, C. P. (1999). Poly(ADP-Ribose) Polymerase Binds with Transcription Enhancer Factor 1 to MCAT1 Elements To Regulate Muscle-Specific Transcription. Molecular and Cellular Biology *19*, 296.

Calses, P. C., Crawford, J. J., Lill, J. R., and Dey, A. (2019). Hippo Pathway in Cancer: Aberrant Regulation and Therapeutic Opportunities. Trends in Cancer *5*, 297-307.

Chamberlain, P. P., and Hamann, L. G. (2019). Development of targeted protein degradation therapeutics. Nat Chem Biol *15*, 937-944.

Chen, Z., Friedrich, G. A., and Soriano, P. (1994). Transcriptional enhancer factor 1 disruption by a retroviral gene trap leads to heart defects and embryonic lethality in mice. Genes & Development *8*, 2293-2301.

Chung, N., Zhang, X. D., Kreamer, A., Locco, L., Kuan, P.-F., Bartz, S., Linsley, P. S., Ferrer, M., and Strulovici, B. (2008). Median Absolute Deviation to Improve Hit Selection for Genome-Scale RNAi Screens. Journal of Biomolecular Screening *13*, 149-158.

Cordenonsi, M., Zanconato, F., Azzolin, L., Forcato, M., Rosato, A., Frasson, C., Inui, M., Montagner, M., Parenti, Anna R., Poletti, A.*, et al.* (2011). The Hippo Transducer TAZ Confers Cancer Stem Cell-Related Traits on Breast Cancer Cells. Cell *147*, 759-772.

Dey, A., Varelas, X., and Guan, K.-L. (2020). Targeting the Hippo pathway in cancer, fibrosis, wound healing and regenerative medicine. Nature Reviews Drug Discovery *19*, 480-494.

Dong, J., Feldmann, G., Huang, J., Wu, S., Zhang, N., Comerford, S. A., Gayyed, Mariana F., Anders, R. A., Maitra, A., and Pan, D. (2007). Elucidation of a Universal Size-Control Mechanism in Drosophila and Mammals. Cell *130*, 1120-1133.

Emsley, P., and Cowtan, K. (2004). Coot: model-building tools for molecular graphics. Acta crystallographica Section D, Biological crystallography *60*, 2126-2132.

Evans, P. (2006). Scaling and assessment of data quality. Acta Crystallographica Section D *62*, 72-82.

Evans, P. R., and Murshudov, G. N. (2013). How good are my data and what is the resolution? Acta crystallographica Section D, Biological crystallography *69*, 1204-1214.

Fan, Q., Wang, Q., Cai, R., Yuan, H., and Xu, M. (2020). The ubiquitin system: orchestrating cellular signals in non-small-cell lung cancer. Cellular & Molecular Biology Letters *25*, 1.

Halder, G., and Johnson, R. L. (2011). Hippo signaling: growth control and beyond. Development *138*, 9.

Han, X., Zhao, L., Xiang, W., Qin, C., Miao, B., Xu, T., Wang, M., Yang, C. Y., Chinnaswamy, K., Stuckey, J., and Wang, S. (2019). Discovery of Highly Potent and Efficient PROTAC Degraders of Androgen Receptor (AR) by Employing Weak Binding Affinity VHL E3 Ligase Ligands. J Med Chem *62*, 11218-11231.

Holden, J. K., Crawford, J. J., Noland, C. L., Schmidt, S., Zbieg, J. R., Lacap, J. A., Zang, R., Miller, G. M., Zhang, Y., Beroza, P.*, et al.* (2020). Small Molecule Dysregulation of TEAD Lipidation Induces a Dominant-Negative Inhibition of Hippo Pathway Signaling. Cell Rep *31*, 107809.

Huh, H. D., Kim, D. H., Jeong, H.-S., and Park, H. W. (2019). Regulation of TEAD Transcription Factors in Cancer Biology. Cells *8*, 600.

Jungmichel, S., Rosenthal, F., Altmeyer, M., Lukas, J., Hottiger, Michael O., and Nielsen, Michael L. (2013). Proteome-wide Identification of Poly(ADP-Ribosyl)ation Targets in Different Genotoxic Stress Responses. Mol Cell *52*, 272-285.

Kabsch, W. (2010). XDS. Acta crystallographica Section D, Biological crystallography *66*, 125-132.

Kamaletdinova, T., Fanaei-Kahrani, Z., and Wang, Z.-Q. (2019). The Enigmatic Function of PARP1: From PARylation Activity to PAR Readers. Cells *8*.

Kaneko, K. J., Kohn, M. J., Liu, C., and DePamphilis, M. L. (2007). Transcription factor TEAD2 is involved in neural tube closure. genesis *45*, 577-587.

Kang, H. C., Lee, Y.-I., Shin, J.-H., Andrabi, S. A., Chi, Z., Gagné, J.-P., Lee, Y., Ko, H. S., Lee, B. D., Poirier, G. G.*, et al.* (2011). Iduna is a poly(ADP-ribose) (PAR)-dependent E3 ubiquitin ligase that regulates DNA damage. Proceedings of the National Academy of Sciences *108*, 14103.

Kapoor, A., Yao, W., Ying, H., Hua, S., Liewen, A., Wang, Q., Zhong, Y., Wu, C.-J., Sadanandam, A., Hu, B., *et al.* (2014). Yap1 Activation Enables Bypass of Oncogenic Kras Addiction in Pancreatic Cancer. Cell *158*, 185-197.
Kim, W., Bennett, Eric J., Huttlin, Edward L., Guo, A., Li, J., Possemato, A., Sowa, Mathew E., Rad, R., Rush, J., Comb, Michael J., *et al.* (2011). Systematic and Quantitative Assessment of the Ubiquitin-Modified Proteome. Mol Cell *44*, 325-340.
Kirkpatrick, D. S., Bustos, D. J., Dogan, T., Chan, J., Phu, L., Young, A., Friedman, L. S., Belvin, M., Song, Q., Bakalarski, C. E., and Hoeflich, K. P. (2013). Phosphoproteomic characterization of DNA damage response in melanoma cells following MEK/PI3K dual inhibition. Proceedings of the National Academy of Sciences *110*, 19426.
König, R., Chiang, C.-y., Tu, B. P., Yan, S. F., DeJesus, P. D., Romero, A., Bergauer, T., Orth, A., Krueger, U., Zhou, Y., and Chanda, S. K. (2007). A probability-based approach for the analysis of large-scale RNAi screens. Nature Methods *4*, 847.
Lee, M.-L., Aliagas, I., Feng, J., Gabriel, T., O'Donnell, T. J., Sellers, B., Wiswedel, B., and Gobbi, A. (2017). Chemalot and chemalot-knime: Command line programs as workflow tools for drug discovery. Journal of Cheminformatics *9*.
Li, X., Wang, W., Wang, J., Malovannaya, A., Xi, Y., Li, W., Guerra, R., Hawke, D. H., Qin, J., and Chen, J. (2015). Proteomic analyses reveal distinct chromatin-associated and soluble transcription factor complexes. Molecular Systems Biology *11*, 775.
Liang, L. (2005). R-sequences: Relative indicators for the rhythm of science. Journal of the American Society for Information Science and Technology *56*, 1045-1049.
Lin, K. C., Park, H. W., and Guan, K.-L. (2017). Regulation of the Hippo Pathway Transcription Factor TEAD. Trends in Biochemical Sciences *42*, 862-872.
Lin, L., Sabnis, A. J., Chan, E., Olivas, V., Cade, L., Pazarentzos, E., Asthana, S., Neel, D., Yan, J. J., Lu, X., *et al.* (2015). The Hippo effector YAP promotes resistance to RAF- and MEK-targeted cancer therapies. Nature Genetics *47*, 250.
Lin, X., and Zhang, D. (1999). Inference in generalized additive mixed modelsby using smoothing splines. Journal of the Royal Statistical Society: Series B (Statistical Methodology) *61*, 381-400.
McCoy, A. J., Grosse-Kunstleve, R. W., Adams, P. D., Winn, M. D., Storoni, L. C., and Read, R. J. (2007). Phaser crystallographic software. Journal of Applied Crystallography *40*, 658-674.
Mesrouze, Y., Meyerhofer, M., Bokhovchuk, F., Fontana, P., Zimmermann, C., Martin, T., Delaunay, C., Izaac, A., Kallen, J., Schmelzle, T., *et al.* (2017). Effect of the acylation of TEAD4 on its interaction with co-activators YAP and TAZ. Protein Science *26*, 2399-2409.
Meyers, R. M., Bryan, J. G., McFarland, J. M., Weir, B. A., Sizemore, A. E., Xu, H., Dharia, N. V., Montgomery, P. G., Cowley, G. S., Pantel, S., *et al.* (2017). Computational correction of copy number effect improves specificity of CRISPR–Cas9 essentiality screens in cancer cells. Nature Genetics *49*, 1779-1784.
Newsome, T. P., Schmidt, S., Dietzl, G., Keleman, K., Åsling, B., Debant, A., and Dickson, B. J. (2000). Trio Combines with Dock to Regulate Pak Activity during Photoreceptor Axon Pathfinding in Drosophila. Cell *101*, 283-294.
Nishioka, N., Inoue, K.-i., Adachi, K., Kiyonari, H., Ota, M., Ralston, A., Yabuta, N., Hirahara, S., Stephenson, R. O., Ogonuki, N., *et al.* (2009). The Hippo Signaling Pathway Components Lats and Yap Pattern Tead4 Activity to Distinguish Mouse Trophectoderm from Inner Cell Mass. Developmental Cell *16*, 398-410.
Nishioka, N., Yamamoto, S., Kiyonari, H., Sato, H., Sawada, A., Ota, M., Nakao, K., and Sasaki, H. (2008). Tead4 is required for specification of trophectoderm in pre-implantation mouse embryos. Mechanisms of Development *125*, 270-283.
Noland, Cameron L., Gierke, S., Schnier, Paul D., Murray, J., Sandoval, Wendy N., Sagolla, M., Dey, A., Hannoush, Rami N., Fairbrother, Wayne J., and Cunningham, Christian N. (2016). Palmitoylation of TEAD Transcription Factors Is Required for Their Stability and Function in Hippo Pathway Signaling. Structure *24*, 179-186.
Pan, D. (2010). The Hippo Signaling Pathway in Development and Cancer. Developmental Cell *19*, 491-505.
Pham, T. H., Hagenbeek, T. J., Lee, H.-J., Li, J., Rose, C. M., Lin, E., Yu, M., Martin, S. E., Piskol, R., Lacap, J. A., *et al.* (2021). Machine-Learning and Chemicogenomics Approach Defines and Predicts Cross-Talk of Hippo and MAPK Pathways. Cancer Discovery *11*, 778-793.
Rush, J., Moritz, A., Lee, K. A., Guo, A., Goss, V. L., Spek, E. J., Zhang, H., Zha, X.-M., Polakiewicz, R. D., and Comb, M. J. (2005). Immunoaffinity profiling of tyrosine phosphorylation in cancer cells. Nature Biotechnology *23*, 94-101.
Sakamoto, K. M., Kim, K. B., Kumagai, A., Mercurio, F., Crews, C. M., and Deshaies, R. J. (2001). Protacs: chimeric molecules that target proteins to the Skp1-Cullin-F box complex for ubiquitination and degradation. Proceedings of the National Academy of Sciences of the United States of America *98*, 8554-8559.

Sanchez-Vega, F., Mina, M., Armenia, J., Chatila, W. K., Luna, A., La, K. C., Dimitriadoy, S., Liu, D. L., Kantheti, H. S., Saghafinia, S.*, et al.* (2018). Oncogenic Signaling Pathways in The Cancer Genome Atlas. Cell *173*, 321-337.e310.
Scheepstra, M., Hekking, K. F. W., van Hijfte, L., and Folmer, R. H. A. (2019). Bivalent Ligands for Protein Degradation in Drug Discovery. Comput Struct Biotechnol J *17*, 160-176.
Schrödinger, L., New York, NY, (2019). Schrödinger Release 2019-4: .
Shi, Z., He, F., Chen, M., Hua, L., Wang, W., Jiao, S., and Zhou, Z. (2017). DNA-binding mechanism of the Hippo pathway transcription factor TEAD4. Oncogene *36*, 4362-4369.
Simmonds, A. J., Liu, X., Soanes, K. H., Krause, H. M., Irvine, K. D., and Bell, J. B. (1998). Molecular interactions between Vestigial and Scalloped promote wing formation in Drosophila. Genes & Development *12*, 3815-3820.
Song, S., Honjo, S., Jin, J., Chang, S. S., Scott, A. W., Chen, Q., Kalhor, N., Correa, A. M., Hofstetter, W. L., Albarracin, C. T.*, et al.* (2015). The Hippo Coactivator YAP1 Mediates EGFR Overexpression and Confers Chemoresistance in Esophageal Cancer. Clin Cancer Res *21*, 2580-2590.
Steinhardt, A. A., Gayyed, M. F., Klein, A. P., Dong, J., Maitra, A., Pan, D., Montgomery, E. A., and Anders, R. A. (2008). Expression of Yes-associated protein in common solid tumors. Human Pathology *39*, 1582-1589.
Sudol, M., and Harvey, K. F. (2010). Modularity in the Hippo signaling pathway. Trends in Biochemical Sciences *35*, 627-633.
Tian, W., Yu, J., Tomchick, D. R., Pan, D., and Luo, X. (2010). Structural and functional analysis of the YAP-binding domain of human TEAD2. Proceedings of the National Academy of Sciences of the United States of America *107*, 7293-7298.
Tickle, I. J., Flensburg, C., Keller, P., Paciorek, W., Sharff, A., Vonrhein, C., & Bricogne, G (2017). STARANISO. Cambridge, United Kingdom: Global Phasing Ltd.
Udan, R. S., Kango-Singh, M., Nolo, R., Tao, C., and Halder, G. (2003). Hippo promotes proliferation arrest and apoptosis in the Salvador/Warts pathway. Nature Cell Biology *5*, 914-920.
Vassilev, A., Kaneko, K. J., Shu, H., Zhao, Y., and DePamphilis, M. L. (2001). TEAD/TEF transcription factors utilize the activation domain of YAP65, a Src/Yes-associated protein localized in the cytoplasm. Genes & Development *15*, 1229-1241.
Vonrhein, C., Flensburg, C., Keller, P., Sharff, A., Smart, O., Paciorek, W., Womack, T., and Bricogne, G. (2011). Data processing and analysis with the autoPROC toolbox. Acta crystallographica Section D, Biological crystallography *67*, 293-302.
Wang, W., Li, N., Li, X., Tran, My K., Han, X., and Chen, J. (2015). Tankyrase Inhibitors Target YAP by Stabilizing Angiomotin Family Proteins. Cell Reports *13*, 524-532.
Winn, M. D., Ballard, C. C., Cowtan, K. D., Dodson, E. J., Emsley, P., Evans, P. R., Keegan, R. M., Krissinel, E. B., Leslie, A. G., McCoy, A.*, et al.* (2011). Overview of the CCP4 suite and current developments. Acta crystallographica Section D, Biological crystallography *67*, 235-242.
Xiao, J. H., Davidson, I., Matthes, H., Garnier, J.-M., and Chambon, P. (1991). Cloning, expression, and transcriptional properties of the human enhancer factor TEF-1. Cell *65*, 551-568.
Yagi, R., Kohn, M. J., Karavanova, I., Kaneko, K. J., Vullhorst, D., DePamphilis, M. L., and Buonanno, A. (2007). Transcription factor TEAD4 specifies the trophectoderm lineage at the beginning of mammalian development. Development *134*, 3827.
Yang, C.-S., Jividen, K., Spencer, A., Dworak, N., Ni, L., Oostdyk, L. T., Chatterjee, M., Kuśmider, B., Reon, B., Parlak, M.*, et al.* (2017). Ubiquitin Modification by the E3 Ligase/ADP-Ribosyltransferase Dtx3L/Parp9. Mol Cell *66*, 503-516.e505.
Yang, C. Y., Qin, C., Bai, L., and Wang, S. (2019). Small-molecule PROTAC degraders of the Bromodomain and Extra Terminal (BET) proteins - A review. Drug Discov Today Technol *31*, 43-51.
Yasunami, M., Suzuki, K., and Ohkubo, H. (1996). A Novel Family of TEA Domain-Containing Transcription Factors with Distinct Spatiotemporal Expression Patterns. Biochemical and Biophysical Research Communications *228*, 365-370.
You, I., Erickson, E. C., Donovan, K. A., Eleuteri, N. A., Fischer, E. S., Gray, N. S., and Toker, A. (2020). Discovery of an AKT Degrader with Prolonged Inhibition of Downstream Signaling. Cell Chem Biol *27*, 66-73 e67.
Yu, F.-X., and Guan, K.-L. (2013). The Hippo pathway: regulators and regulations. Genes & Development *27*, 355-371.
Yu, K., Phu, L., Varfolomeev, E., Bustos, D., Vucic, D., and Kirkpatrick, D. S. (2015). Immunoaffinity Enrichment Coupled to Quantitative Mass Spectrometry Reveals Ubiquitin-Mediated Signaling Events. Journal of Molecular Biology *427*, 2121-2134.
Zanconato, F., Cordenonsi, M., and Piccolo, S. (2016). YAP/TAZ at the Roots of Cancer. Cancer cell *29*, 783-803.

Zhang, H., Liu, C.-Y., Zha, Z.-Y., Zhao, B., Yao, J., Zhao, S., Xiong, Y., Lei, Q.-Y., and Guan, K.-L. (2009). TEAD Transcription Factors Mediate the Function of TAZ in Cell Growth and Epithelial-Mesenchymal Transition. Journal of Biological Chemistry *284*, 13355-13362.
Zhang, Y., Liu, S., Mickanin, C., Feng, Y., Charlat, O., Michaud, G. A., Schirle, M., Shi, X., Hild, M., Bauer, A.*, et al.* (2011). RNF146 is a poly(ADP-ribose)-directed E3 ligase that regulates axin degradation and Wnt signalling. Nature Cell Biology *13*, 623-629.
Zhang, Y., Wang, J., Ding, M., and Yu, Y. (2013). Site-specific characterization of the Asp- and Glu-ADP-ribosylated proteome. Nature Methods *10*, 981-984.
Zhao, B., Li, L., Lei, Q., and Guan, K.-L. (2010). The Hippo–YAP pathway in organ size control and tumorigenesis: an updated version. Genes & Development *24*, 862-874.
Zhao, B., Wei, X., Li, W., Udan, R. S., Yang, Q., Kim, J., Xie, J., Ikenoue, T., Yu, J., Li, L.*, et al.* (2007). Inactivation of YAP oncoprotein by the Hippo pathway is involved in cell contact inhibition and tissue growth control. Genes & Development *21*, 2747-2761.
Zhao, B., Ye, X., Yu, J., Li, L., Li, W., Li, S., Yu, J., Lin, J. D., Wang, C.-Y., Chinnaiyan, A. M.*, et al.* (2008). TEAD mediates YAP-dependent gene induction and growth control. Genes & Development *22*, 1962-1971.
Zhou, Z.-d., Chan, C. H.-s., Xiao, Z.-c., and Tan, E.-K. (2011). Ring finger protein 146/Iduna is a Poly(ADP-ribose) polymer binding and PARsylation dependent E3 ubiquitin ligase. Cell Adhesion & Migration *5*, 463-471.

Figure 1

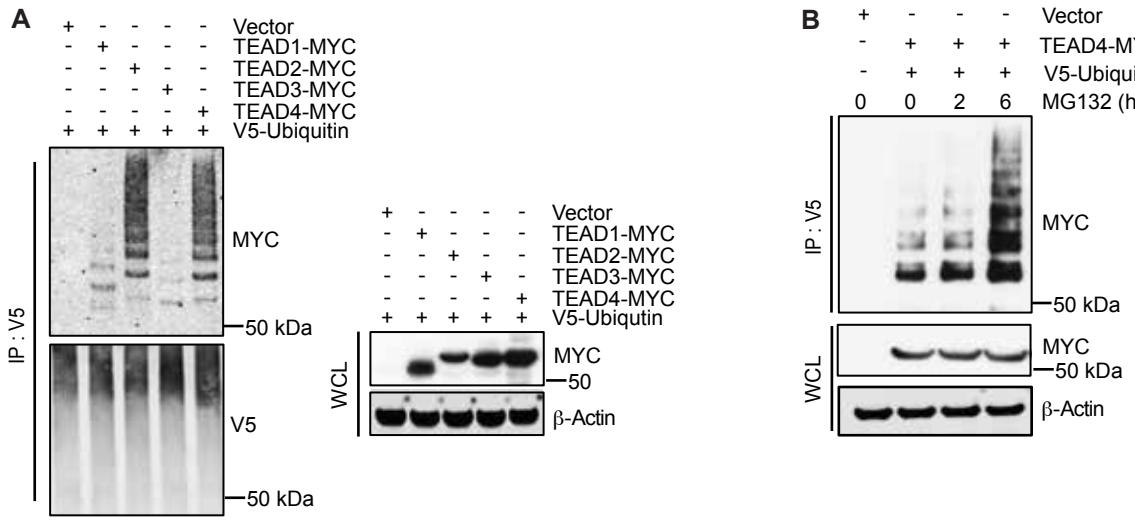

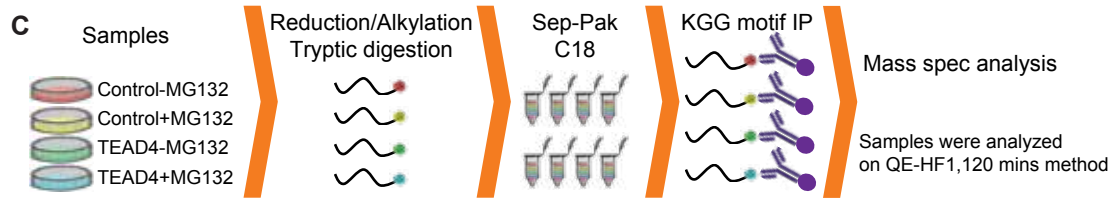

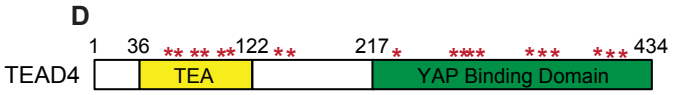

TEAD4 Ubiquitination sites (K)	w/o MG132	w/ MG132
K65	✓	✓
K73	✓	✓
K65 and K73	✓	✓
K86	✓	✓
K96	✓	✓
K116	✓	✓
K118	✓	✓
K116 and K118	✓	✓
K123	✓	✓
K125	✓	✓
K123 and K125	✓	✓
K118, K123 and K125	-	✓
K223	✓	✓
K273	✓	✓
K277	✓	✓
K273 and K277	✓	✓
K278	✓	✓
K282	✓	✓
K278 and K282	✓	✓
K333	-	✓
K339	✓	✓
K344	✓	✓
K339 and K344	✓	✓
K376	✓	✓
K378	✓	✓
K383	✓	✓
K378 and K383	✓	✓

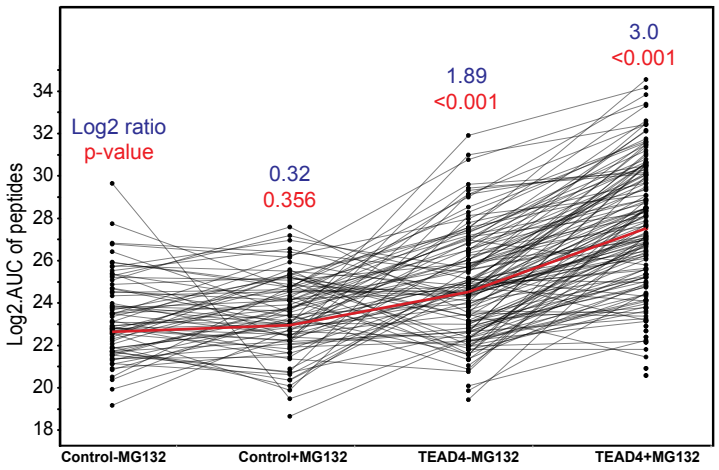

Figure 2

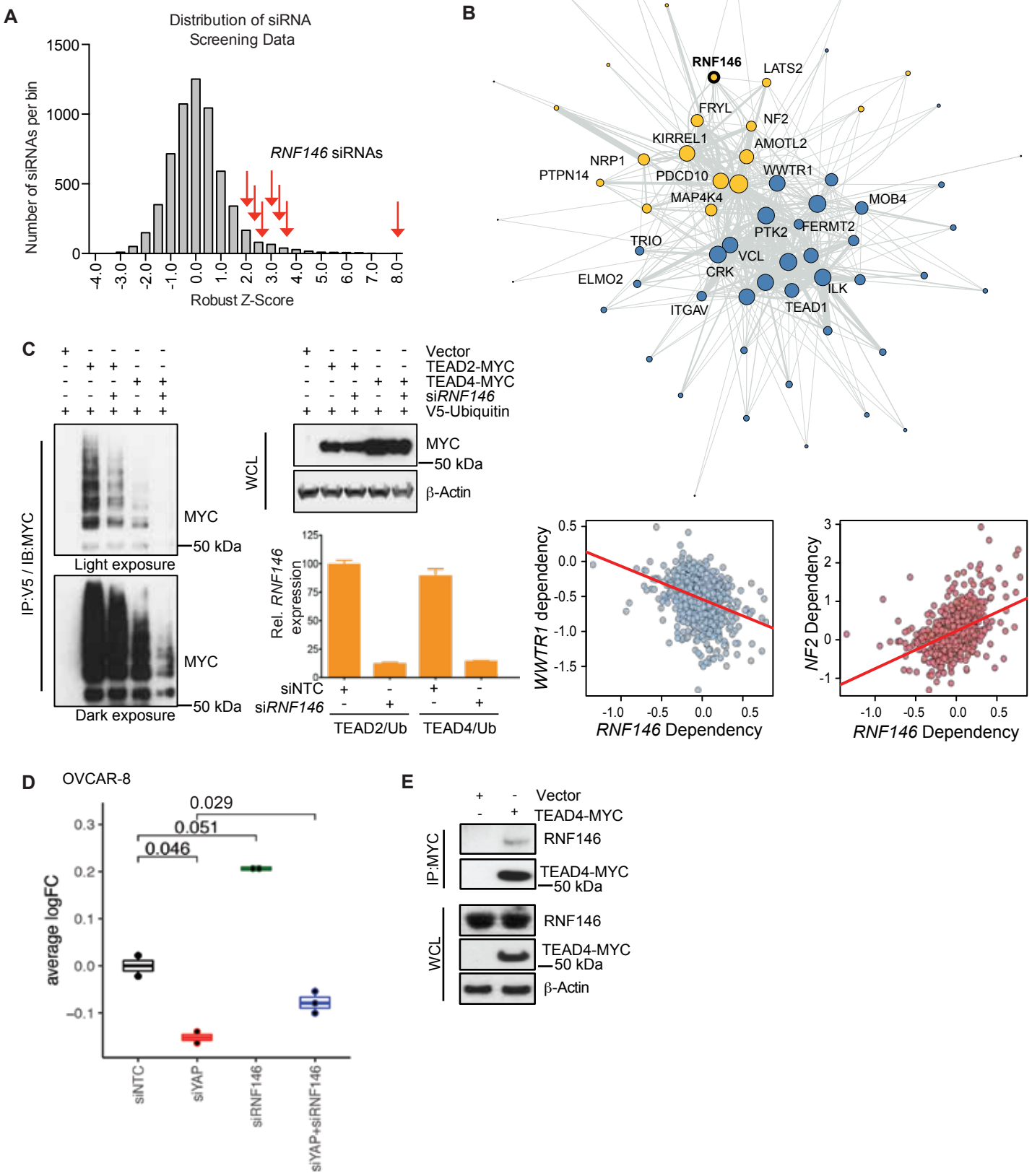
A
Distribution of siRNA Screening Data
Number of siRNAs per bin
1500
1000
500
0
RNF146 siRNAs
-4.0
-3.0
-2.0
-1.0
0.0
1.0
2.0
3.0
4.0
5.0
6.0
7.0
8.0
Robust Z-Score
B
RNF146
LATS2
FRYL
NF2
KIRREL1
AMOTL2
NRP1
PTPN14
PDCD10
WWTR1
MAP4K4
MOB4
PTK2
FERMT2
TRIO
VCL
CRK
ELMO2
ILK
ITGAV
TEAD1
C
Vector
TEAD2-MYC
TEAD4-MYC
siRNF146
V5-Ubiquitin
IP:V5 / IB:MYC
MYC
50 kDa
Light exposure
Dark exposure
WCL
β-Actin
Rel. RNF146 expression
siNTC
siRNF146
TEAD2/Ub
TEAD4/Ub
WWTR1 dependency
RNF146 Dependency
NF2 Dependency
D
OVCAR-8
average logFC
0.029
0.051
0.046
siNTC
siYAP
siRNF146
siYAP+siRNF146
E
Vector
TEAD4-MYC
IP:MYC
RNF146
TEAD4-MYC
50 kDa
WCL
β-Actin

Figure 3

A

Identifier	IgG_ condition1	IP_ condition1	IgG_ condition 2	IP_ condition2
PARP1_ P09874	0	52	0	26
PARP9_ Q9UKK3	1	9	1	14

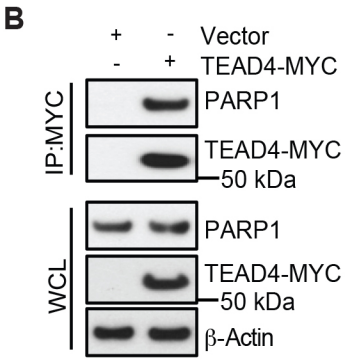

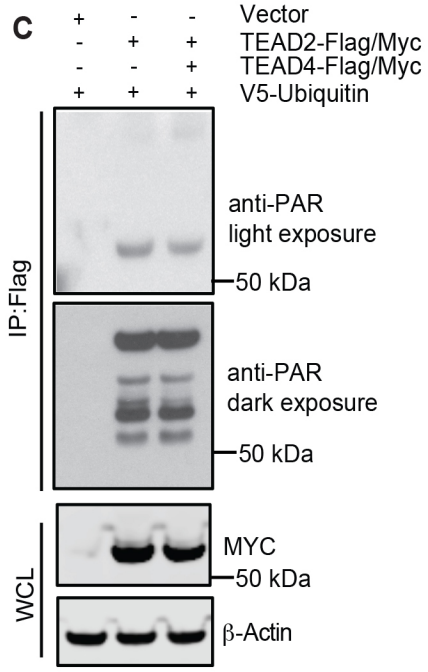

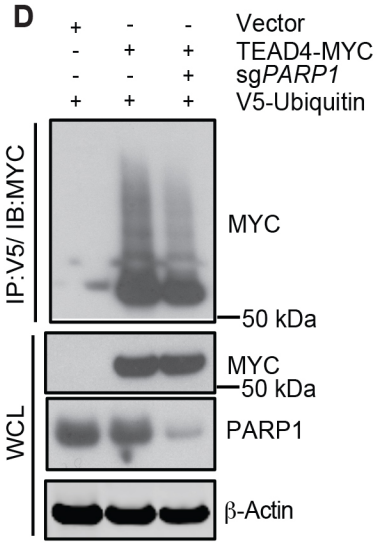

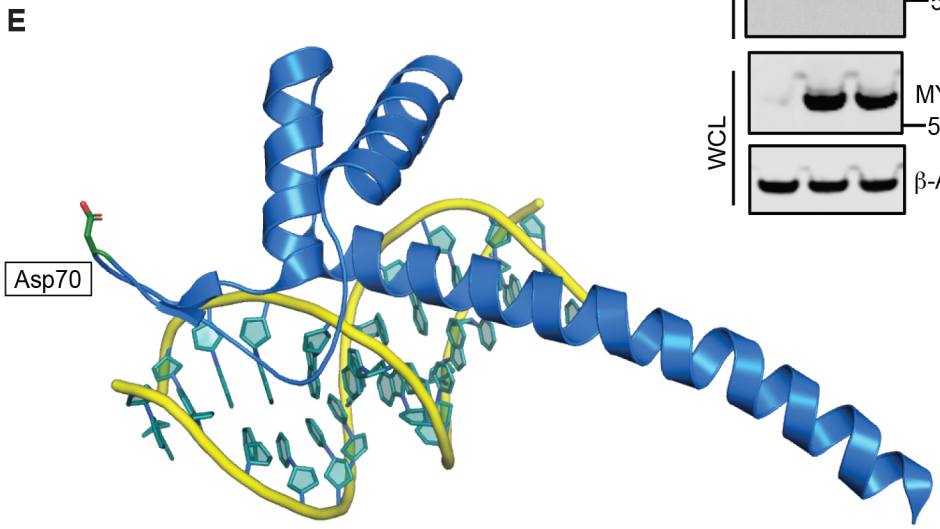

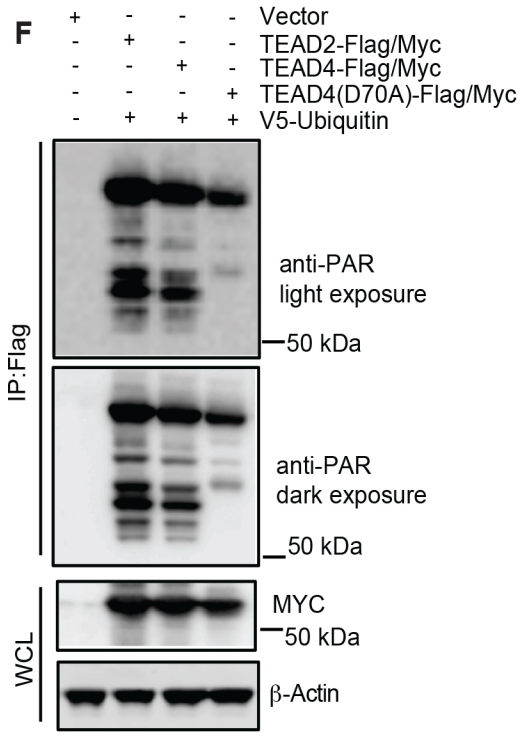

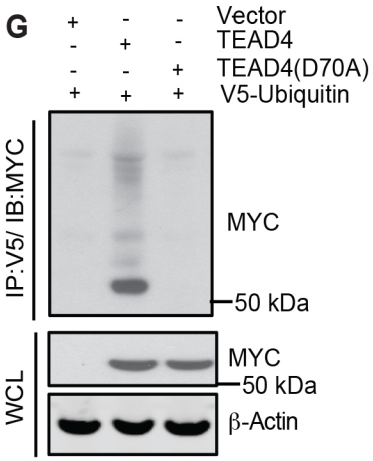

Figure 4

A

```
sp|P28347|TEAD1    -----AENM--ERMSDSADKPIDNDAEGVWSPDIEQSFQEALAIYPPCGRRKIILSDEGKMYG
sp|Q15562|TEAD2    -----SEEG--TGGSEGAGGDGGPDAEGVWSPDIEQSFQEALAIYPPCGRRKIILSDEGKMYG
sp|Q99594|TEAD3    -----GEAR--EDGPEGLDKGLDNDAEGVWSPDIEQSFQEALAIYPPCGRRKIILSDEGKMYG
sp|Q15561|TEAD4    -----GSTA--SGGSQALDKPIDNDAEGVWSPDIEQSFQEALAIYPPCGRRKIILSDEGKMYG
sp|P30052|SCAL_    GSMVDSKNLDVGDMSDDEKDLSSADAEGVWSPDIEQSFQEALSIYPPCGRRKIILSDEGKMYG
```

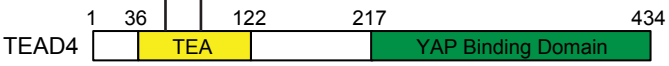

B

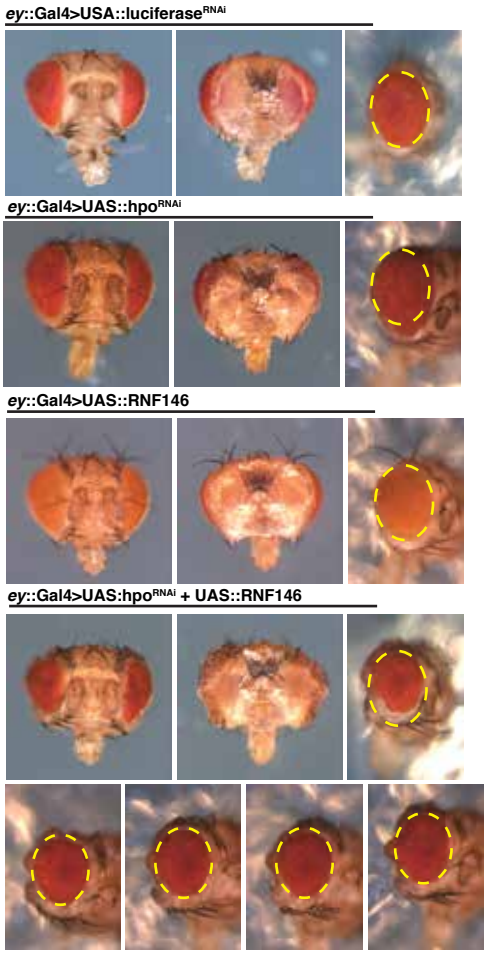

D

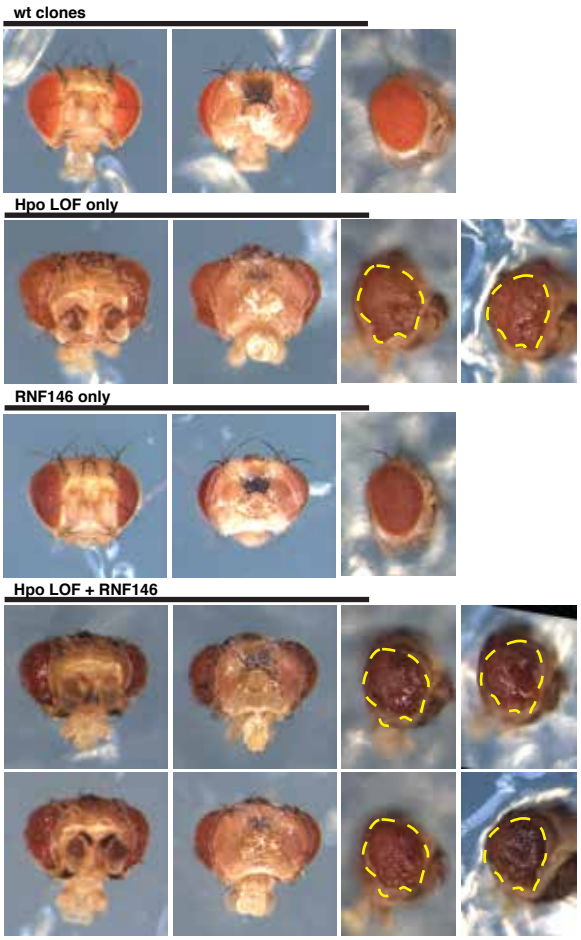

C

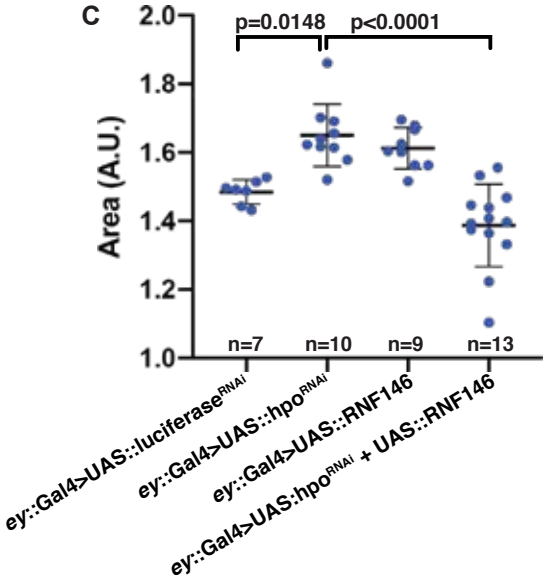

E

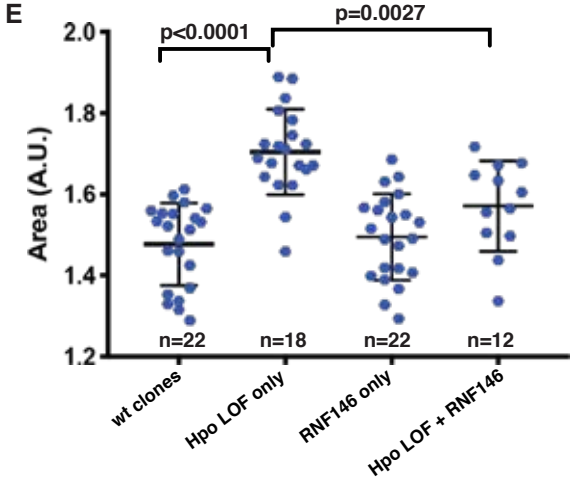

Figure 5

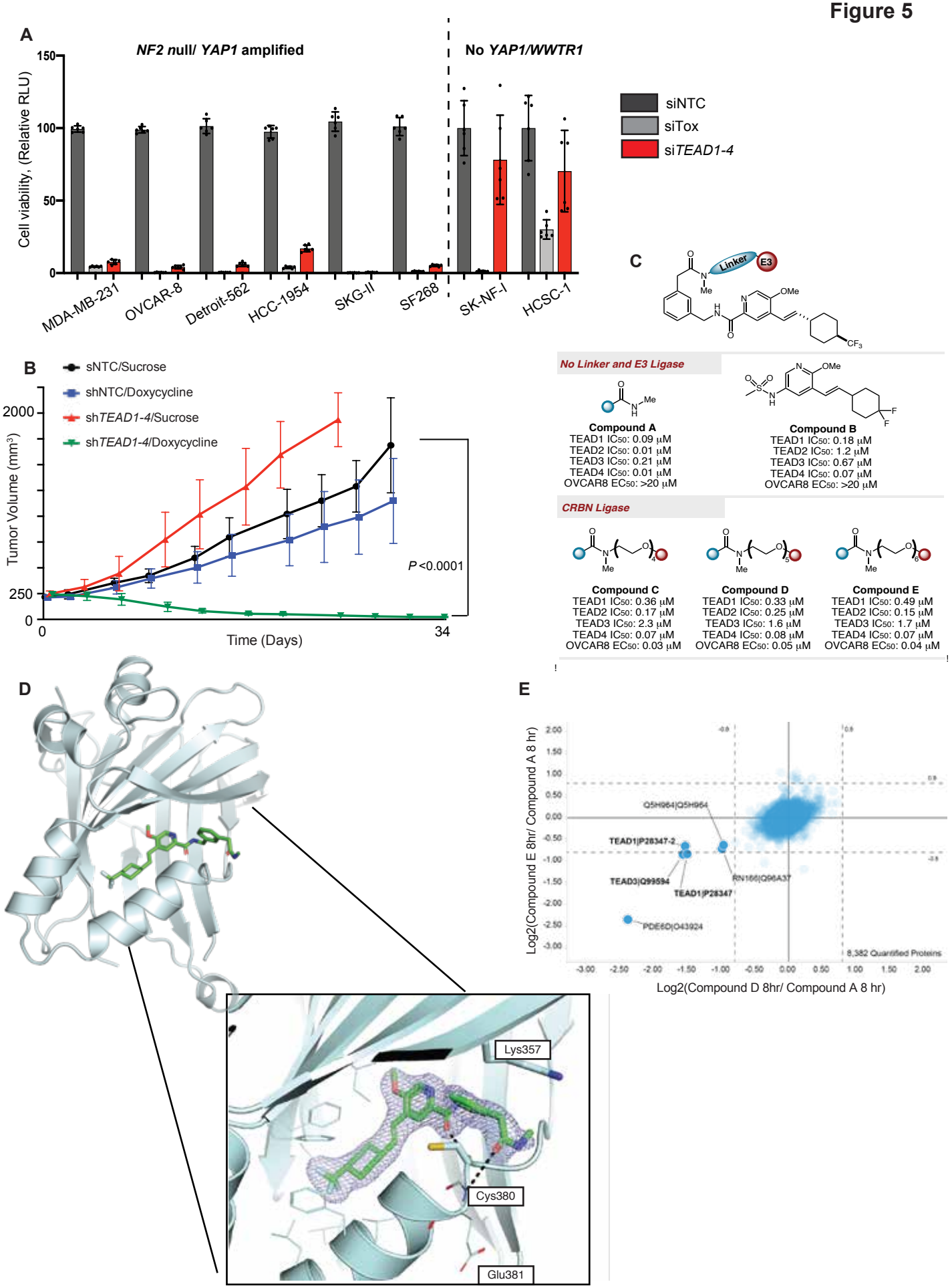
A
NF2 null/ YAP1 amplified
No YAP1/WWTR1
Cell viability, (Relative RLU)
150
100
50
0
MDA-MB-231
OVCAR-8
Detroit-562
HCC-1954
SKG-II
SF268
SK-NF-I
HCSC-1
siNTC
siTox
siTEAD1-4
B
sNTC/Sucrose
shNTC/Doxycycline
shTEAD1-4/Sucrose
shTEAD1-4/Doxycycline
Tumor Volume (mm3)
2000
250
0
P<0.0001
0
34
Time (Days)
C
Linker
E3
OMe
CF3
No Linker and E3 Ligase
Compound A
TEAD1 IC50: 0.09 μM
TEAD2 IC50: 0.01 μM
TEAD3 IC50: 0.21 μM
TEAD4 IC50: 0.01 μM
OVCAR8 EC50: >20 μM
Compound B
TEAD1 IC50: 0.18 μM
TEAD2 IC50: 1.2 μM
TEAD3 IC50: 0.67 μM
TEAD4 IC50: 0.07 μM
OVCAR8 EC50: >20 μM
CRBN Ligase
Compound C
TEAD1 IC50: 0.36 μM
TEAD2 IC50: 0.17 μM
TEAD3 IC50: 2.3 μM
TEAD4 IC50: 0.07 μM
OVCAR8 EC50: 0.03 μM
Compound D
TEAD1 IC50: 0.33 μM
TEAD2 IC50: 0.25 μM
TEAD3 IC50: 1.6 μM
TEAD4 IC50: 0.08 μM
OVCAR8 EC50: 0.05 μM
Compound E
TEAD1 IC50: 0.49 μM
TEAD2 IC50: 0.15 μM
TEAD3 IC50: 1.7 μM
TEAD4 IC50: 0.07 μM
OVCAR8 EC50: 0.04 μM
D
Lys357
Cys380
Glu381
E
Log2(Compound E 8hr/ Compound A 8 hr)
Log2(Compound D 8hr/ Compound A 8 hr)
Q5H964|Q5H964
TEAD1|P28347-2
TEAD3|Q99594
TEAD1|P28347
PDE6D|O43924
8,382 Quantified Proteins

Figure 6

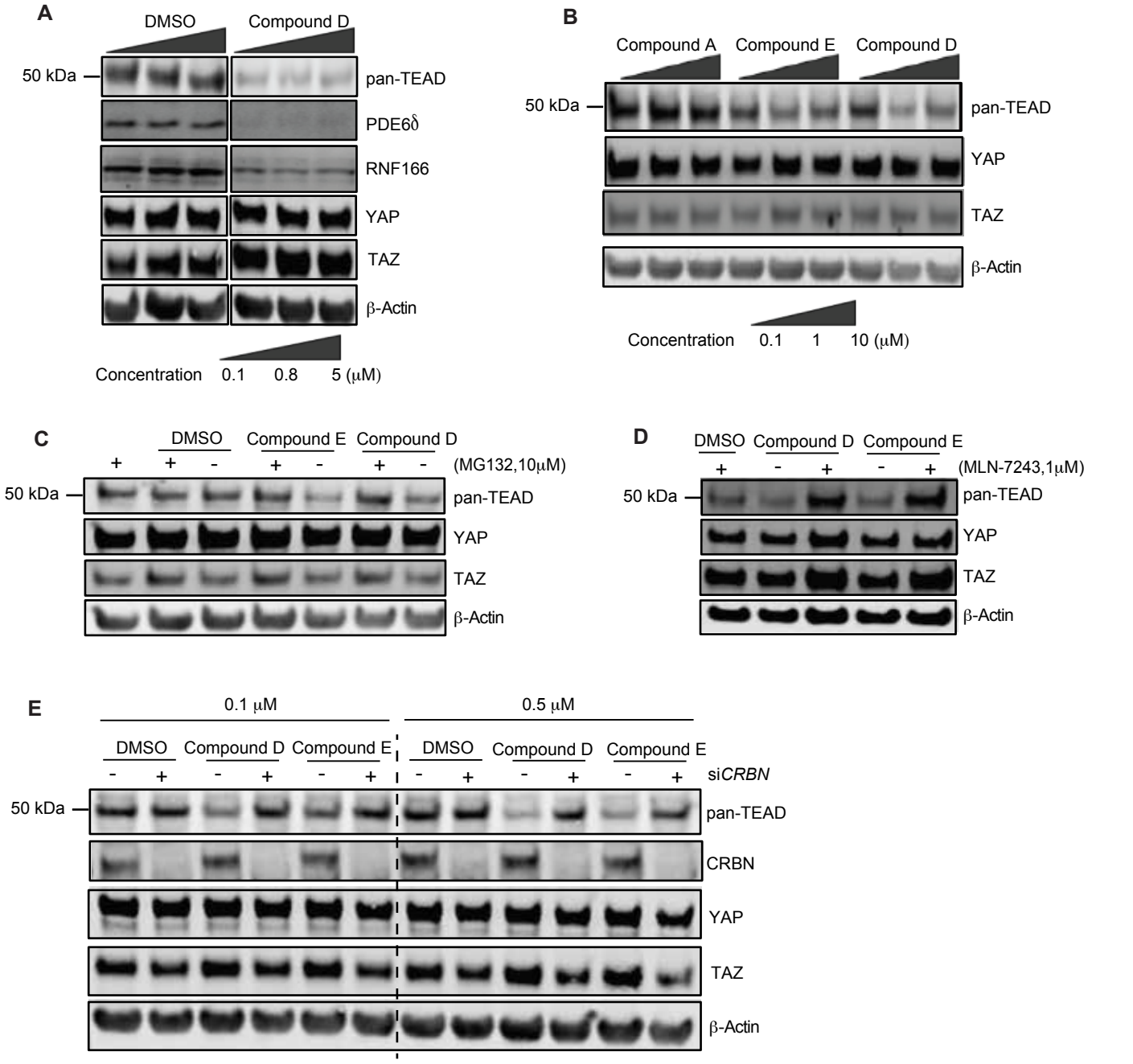
A
DMSO
Compound D
50 kDa
pan-TEAD
PDE6δ
RNF166
YAP
TAZ
β-Actin
Concentration 0.1 0.8 5 (μM)
B
Compound A
Compound E
Compound D
50 kDa
pan-TEAD
YAP
TAZ
β-Actin
Concentration 0.1 1 10 (μM)
C
DMSO
Compound E
Compound D
+ + - + - + - (MG132,10μM)
50 kDa
pan-TEAD
YAP
TAZ
β-Actin
D
DMSO
Compound D
Compound E
+ - + - + (MLN-7243,1μM)
50 kDa
pan-TEAD
YAP
TAZ
β-Actin
E
0.1 μM
0.5 μM
DMSO
Compound D
Compound E
DMSO
Compound D
Compound E
- + - + - + - + - + - + siCRBN
50 kDa
pan-TEAD
CRBN
YAP
TAZ
β-Actin

Figure 7

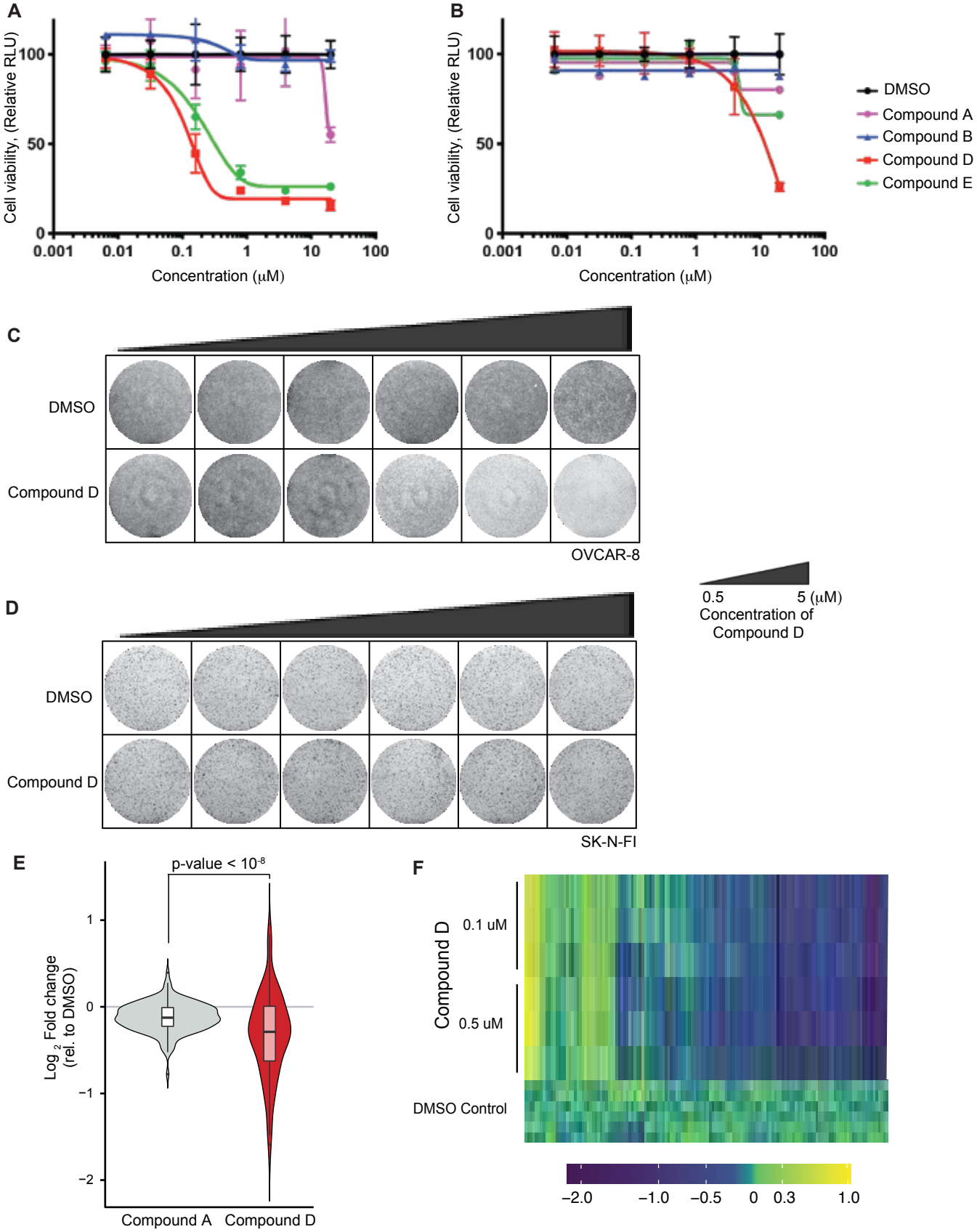
A
Cell viability, (Relative RLU)
100
50
0
0.001
0.01
0.1
1
10
100
Concentration (μM)
B
Cell viability, (Relative RLU)
100
50
0
0.001
0.01
0.1
1
10
100
Concentration (μM)
DMSO
Compound A
Compound B
Compound D
Compound E
C
DMSO
Compound D
OVCAR-8
0.5
5 (μM)
Concentration of
Compound D
D
DMSO
Compound D
SK-N-FI
E
p-value < 10-8
Log 2 Fold change
(rel. to DMSO)
1
0
−1
−2
Compound A
Compound D
F
Compound D
0.1 uM
0.5 uM
DMSO Control
−2.0
−1.0
−0.5
0
0.3
1.0

Figure 8

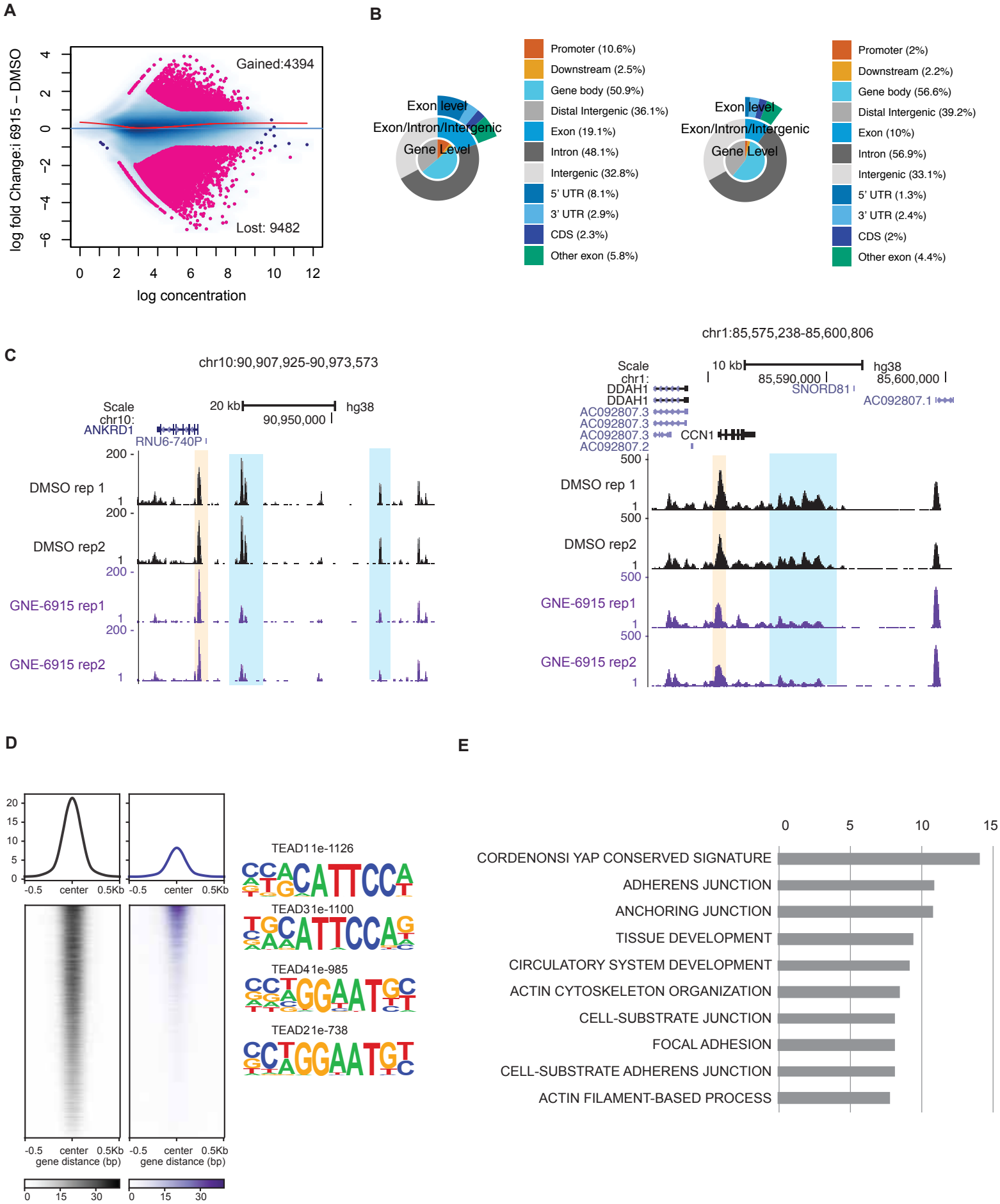
A
Gained:4394
Lost: 9482
log fold Change:i 6915 – DMSO
log concentration
B
Exon level
Exon/Intron/Intergenic
Gene Level
Promoter (10.6%)
Downstream (2.5%)
Gene body (50.9%)
Distal Intergenic (36.1%)
Exon (19.1%)
Intron (48.1%)
Intergenic (32.8%)
5' UTR (8.1%)
3' UTR (2.9%)
CDS (2.3%)
Other exon (5.8%)
Promoter (2%)
Downstream (2.2%)
Gene body (56.6%)
Distal Intergenic (39.2%)
Exon (10%)
Intron (56.9%)
Intergenic (33.1%)
5' UTR (1.3%)
3' UTR (2.4%)
CDS (2%)
Other exon (4.4%)
C
chr10:90,907,925-90,973,573
Scale
chr10:
20 kb
90,950,000
hg38
ANKRD1
RNU6-740P
DMSO rep 1
DMSO rep2
GNE-6915 rep1
GNE-6915 rep2
chr1:85,575,238-85,600,806
Scale
chr1:
10 kb
85,590,000
85,600,000
hg38
DDAH1
DDAH1
AC092807.3
AC092807.3
AC092807.3
AC092807.2
CCN1
SNORD81
AC092807.1
DMSO rep 1
DMSO rep2
GNE-6915 rep1
GNE-6915 rep2
D
-0.5
center
0.5Kb
gene distance (bp)
TEAD11e-1126
TEAD31e-1100
TEAD41e-985
TEAD21e-738
E
CORDENONSI YAP CONSERVED SIGNATURE
ADHERENS JUNCTION
ANCHORING JUNCTION
TISSUE DEVELOPMENT
CIRCULATORY SYSTEM DEVELOPMENT
ACTIN CYTOSKELETON ORGANIZATION
CELL-SUBSTRATE JUNCTION
FOCAL ADHESION
CELL-SUBSTRATE ADHERENS JUNCTION
ACTIN FILAMENT-BASED PROCESS